Physics of Fluids

RESEARCH ARTICLE | JANUARY 09 2023

Nucleation and cavitation inception in high Reynolds number shear layers

Special Collection: Cavitation

E. S. C. Allan ; L. Barbaca ; J. A. Venning; P. S. Russell ; B. W. Pearce ; P. A. Brandner

Physics of Fluids 35, 013317 (2023)
https://doi.org/10.1063/5.0132054

Physics of Fluids ARTICLE scitation.org/journal/phf

Nucleation and cavitation inception in high Reynolds number shear layers

Cite as: Phys. Fluids **35**, 013317 (2023); doi: 10.1063/5.0132054
Submitted: 26 October 2022 · Accepted: 21 December 2022 ·
Published Online: 9 January 2023

E. S. C. Allan, L. Barbaca,[a] J. A. Venning, P. S. Russell, B. W. Pearce, and P. A. Brandner

AFFILIATIONS

Cavitation Research Laboratory, Australian Maritime College, University of Tasmania, Launceston, Tasmania 7250, Australia

Note: This paper is part of the special topic, Cavitation.

[a]**Author to whom correspondence should be addressed:** Luka.Barbaca@utas.edu.au

ABSTRACT

The influence of nucleation on cavitation inception in a high Reynolds number shear layer in the wake of a backward-facing step was experimentally investigated in a water tunnel. The flow was investigated for two nuclei populations: the one naturally occurring in the water and for the water artificially seeded with monodisperse nuclei. Incipient events were observed to form in stretched quasi-streamwise vortices. The collapse of an incipient cavity resulted in a microbubble cloud dispersed into the shear layer and the step re-circulation zone. These microbubbles, generally larger than those naturally occurring in the water, act as preferential sites for re-nucleation, triggering the formation of developed cavitation. This phenomenon rendered statistical characterization of cavitation inception impractical for the natural nuclei population. The re-nucleation issue was addressed by seeding the flow with a population of large monodisperse nuclei, with a critical pressure higher than that of cavitation products. Spatial distribution of the nuclei within the seeded plume was characterized using a volumetric measurement based on Mie-scattering imaging. The ability to discern individual incipient events enabled examination of the effect of cavitation number and the nuclei injection rate on the inception event rate. The event rate was found to follow a power law with cavitation number and vary linearly with the injection rate. Mapping of spatial distribution of cavitation susceptibility was obtained by combining the spatial distributions of incipient events and nuclei concentration. The current work provides a valuable dataset for the development of computational tools for modeling of cavitation inception in nucleated flows.

I. INTRODUCTION

The occurrence of cavitation generally has a detrimental effect on the performance of naval platforms, particularly their acoustic signature. As the noise level generated during the collapse of cavitation bubbles can be significantly higher than that in non-cavitating conditions, investigation of the underlying physics involved in cavitation inception is of great importance.

The area of a naval platform particularly susceptible to cavitation is that in the vicinity of the propulsor. The flow around the propulsor is characterized by a series of vortical systems undergoing complex interactions resulting in an unsteady pressure field. Modeling the flow around a propulsor is a challenging and expensive task, and to gain fundamental understanding of the physical processes and phenomena involved with vortex interactions, it is beneficial to study a canonical flow topology. An example of flow topology featuring complex vortical interactions is that associated with the turbulent shear layers in the wake of a backward-facing step (BFS).

Since the pioneering work of Kermeen and Parkin (1957), cavitation inception in turbulent shear layers has received considerable interest, and the topic has been reviewed by Arndt (2002). The turbulent shear layer developing in the wake of a BFS consists of primary spanwise vortices and weaker vortical braids of quasi-streamwise orientation (Bernal and Roshko, 1986; Lasheras *et al.*, 1986). Previous studies have shown that due to complex interactions of the vortical systems, the weaker quasi-streamwise vortices (QSV) undergo unsteady stretching, leading to instantaneous secondary vortex core pressure values much lower than the mean values in the cores of the nominally stronger primary vortices (Katz and O'Hern, 1986; O'Hern, 1990; and Iyer and Ceccio, 2002).

The stochastic nature of the unsteady pressure fluctuations makes the accurate characterization of the instantaneous pressure field challenging, but recent advances in experimental techniques (Agarwal *et al.*, 2020; 2021) and numerical modeling (Brandao *et al.*, 2020; Brandao and Mahesh, 2022) have contributed to the better understanding of this aspect of the underlying flow physics.

A common misconception is that cavitation only occurs once the local pressure within the flow reaches water vapor saturation pressure. However, studies have shown that in majority of conditions, the water can withstand considerable tension (Temperley and Chambers, 1946), and for cavitation inception to occur, it is necessary that the water contains sites of weakness, also termed cavitation "nuclei."

The nature of nuclei in the oceans remains uncertain and, while they are predominantly found in the form of gas microbubbles, a host of organic and inorganic chemical species, surfactants, and microbial life found in the oceans add to the complexity of the ocean nuclei content (Stramski *et al.*, 2004). Notwithstanding the effect the impurities and chemicals have on nuclei strength and their creation and destruction process, all nuclei, irrespective of their origin, can be characterized using a nuclei critical pressure, i.e., the pressure at which they become activated.

Emulating the exact composition of the ocean nuclei population in a hydrodynamic facility would be a complex and impractical task, further exacerbated by the uncertainties in the ocean nuclei measurements. A more practical method of studying the effect of nuclei content on cavitation in a laboratory setting is to use filtered demineralized water and then model the ocean nuclei population critical pressure probability distribution by altering the water microbubble content.

Microbubbles are characterized by a size-dependent critical pressure, below which the equilibrium of a microbubble becomes unstable. This can be derived from consideration of the equilibrium of bubble internal and external pressures and the surface tension assuming isothermal internal gas behavior and no mass transfer via phase change or diffusion (Franc and Michel, 2004). A bubble undergoes explosive growth once exposed to the critical pressure, subsequently filling with vapor, leading to rapid development of macroscopic cavitation.

The nuclei concentration scales with the cube of the length scale and concentrations of several orders of magnitude higher than those in the oceans are required to achieve the correct nuclei scaling in model test facilities. Historically, the water nuclei content in the facilities has been controlled indirectly via the water dissolved gas content (Arndt, 2002; Chang *et al.*, 2012); however, advent of the new generation of hydrodynamic facilities is enabling more rigorous direct control of microbubble content. With the recent advances in control of the water nuclei content in model testing, it has been shown that varying levels of nuclei populations can significantly affect cavitation inception (Khoo *et al.*, 2020a; 2021; Russell *et al.*, 2022) as well as the dynamics of developed cavitation (Brandner *et al.*, 2022; Venning *et al.*, 2022).

The Cavitation Research Laboratory (CRL) water tunnel at the Australian Maritime College (AMC) is one of a few facilities worldwide where the water microbubble content can be rigorously controlled. The tunnel incorporates design features and ancillary systems for continuous injection and removal of microbubbles, enabling strict control of the test section nuclei content. In order to study nucleation effects, all the nuclei larger than 10 μm in diameter are removed from the water, which can then be artificially seeded with a controlled microbubble population. Microbubble populations of interest for cavitation modeling range over several orders of magnitude in both concentration and size. Examples of the nuclei populations available at the AMC water tunnel are shown in Fig. 1 as non-cumulative size distributions.

The most sparse population, marked in Fig. 1 with dark red symbols, is representative of the naturally occurring or background nuclei population ever present in the tunnel water. This population is characterized by a stochastic size and spatial distributions, which add to the complexity of cavitation inception characterization. The stochastic

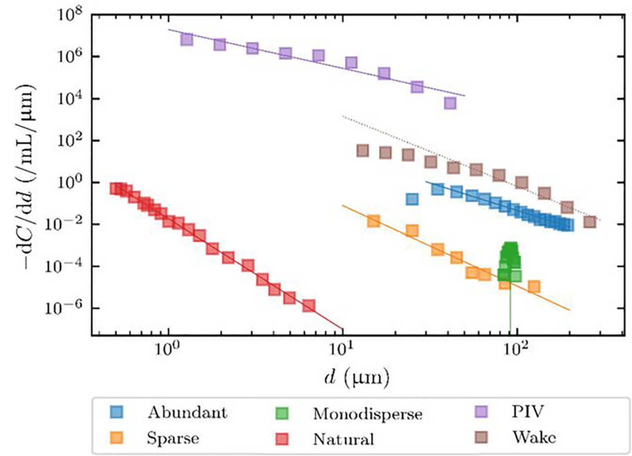

FIG. 1. Nuclei distribution graph showing the bubble diameter, d, and non-cumulative concentration, $\mathrm{d}C/\mathrm{d}d$, for typical nuclei/microbubble populations available at the AMC water tunnel.

character of the nuclei content can be reduced by seeding the tunnel water with a monodisperse microbubble population (green symbols in Fig. 1), i.e., where all the bubbles are of the same size and equally susceptible to cavitation (Franc and Michel, 2004). Alternatively, for applications where higher nuclei concentrations are needed, the water can be seeded with polydisperse microbubble populations, i.e., where the bubbles are distributed across a range of sizes. The bounds of polydisperse populations available at the AMC are denoted with orange (sparse) and blue (abundant) symbols in Fig. 1. Additional populations of interest shown in Fig. 1 include the microbubble content in the wake of a cavitating body (brown symbols) (Russell *et al.*, 2018) and the artificially generated populations of small microbubbles in high concentration (purple symbols) used as tracers for Bubble Image Velocimetry (BIV) (Barbaca *et al.*, 2021).

Within the scope of the current study, the influence of nucleation on cavitation inception in the shear layers in the wake of a BFS is characterized using two nuclei populations. The flow was investigated for the natural nuclei population and for the water artificially seeded with monodisperse nuclei. Further understanding of the stochastic nature of the nuclei content is gained by seeding the flow through a single injection point (targeted seeding) on the BFS surface and statistically characterizing the spatial distribution of the nuclei within the resulting plume using a volumetric Mie-Scattering Imaging (MSI) nuclei measurement technique (Russell *et al.*, 2020a; 2020b). High-speed imaging is used to map the probability density function (PDF) of spatial distribution of incipient cavitation events, which combined with the PDF of spatial distribution of nuclei, is used to obtain a statistical spatial distribution of cavitation susceptibility in the shear layer in the wake of a BFS.

II. EXPERIMENTAL APPROACH

The experiments were performed in the variable pressure water tunnel at the University of Tasmania. The tunnel test section is $0.6 \times 0.6\,\mathrm{m}^2$ at the entrance, by 2.6 m long. The test section ceiling is horizontal with the floor sloping 20 mm over the length to maintain nominally constant speed and a zero streamwise pressure gradient. The operating velocity and pressure are controlled independently, with ranges from 2 to 12 m/s and 4 to 400 kPa absolute, respectively. The tunnel is 365 m^3 and is filled with demineralized water. Optical access is provided through acrylic windows on each side of the test section.

The test section absolute pressure is measured, depending on the value, from high or low range Siemens SITRANS P absolute pressure transducers, models 7MF4333–1FA02–2AB1 (range 0–130 kPa) and 7MF4333–1GA02–2AB1 (range 0–400 kPa), with estimated precision of 0.13 and 0.48 kPa, respectively. The test section velocity is measured from the calibrated contraction differential pressure. Depending on the value, either a high or low range Siemens SITRANS P differential pressure transducers, models 7MF4333–1DA02–2AB1-Z (range 0–25 kPa) and 7MF4333–1FA02–2AB1-Z (range 0–160 kPa), are used with estimated precision of 0.007 and 0.018 m/s, respectively. The dissolved gas content of the water is measured using an Endress+Hauser OxyMax WCOS 41 membrane sensor. Further details on the facility can be found in Brandner *et al.* (2006) and (2007).

The experimental setup has been developed to study cavitation inception in the shear layer formed in the wake of a nominally two-dimensional, i.e., spanning the whole test section width, BFS, which is schematically represented in Fig. 2. The model is machined out of three $1000 \times 600 \times 40\,\text{mm}^3$ PVC sheets glued together to form a 120 mm thick block. The width of the model, w, is 598 mm, ensuring a 1 mm gap between the model and the test section sides. The height of the model is $h = 100$ mm, resulting with the expansion ratio $ER = H/(H - h) = 1.2$ and aspect ratio $AR = w/h \approx 6$. The model consists of a 800 mm (L_R) long upstream ramp described by a fifth-order polynomial equation, $\frac{y}{L_R} = 0.75(\frac{x}{L_R})^5 - 1.875(\frac{x}{L_R})^4 + 1.25(\frac{x}{L_R})^3$, ensuring that the first and second derivative at the curve edges are equal to zero to prevent undesirable pressure gradients. Due to mechanical considerations, the upstream end of the ramp is truncated to 520 mm and a 100 mm long stainless steel linear ramp is attached upstream, resulting with the ramp height of 1.5 mm at the leading edge. Overall length of the ramp, including the PVC and stainless steel section (L_1) is $\approx$620 mm. Downstream of the ramp is a 200 mm (L_2) long horizontal section. The aft part of the model is equipped with two penetrations. The upstream penetration, located 205 mm upstream of the step is 1.6 mm in diameter and is used as the injection port for targeted nuclei seeding. The downstream penetration, located 25 mm upstream of the step is 25 mm in diameter, and is used for boundary layer measurements.

Boundary layer mean velocities were measured on the test section vertical center plane using a 0.7 mm outside, by 0.4 mm inside, diameter total head tube. The tube was mounted on a 6 mm diameter cylindrical stem tapering to the 0.7 mm probe head, protruding through the step model penetration. The total head tube was traversed using an automated linear traverse incorporating a THK LM Guide Actuator Model KR26 with an estimated precision of 3 μm. The reference static pressure was measured separately using a 1 mm diameter wall static pressure tapping mounted through the step model penetration after

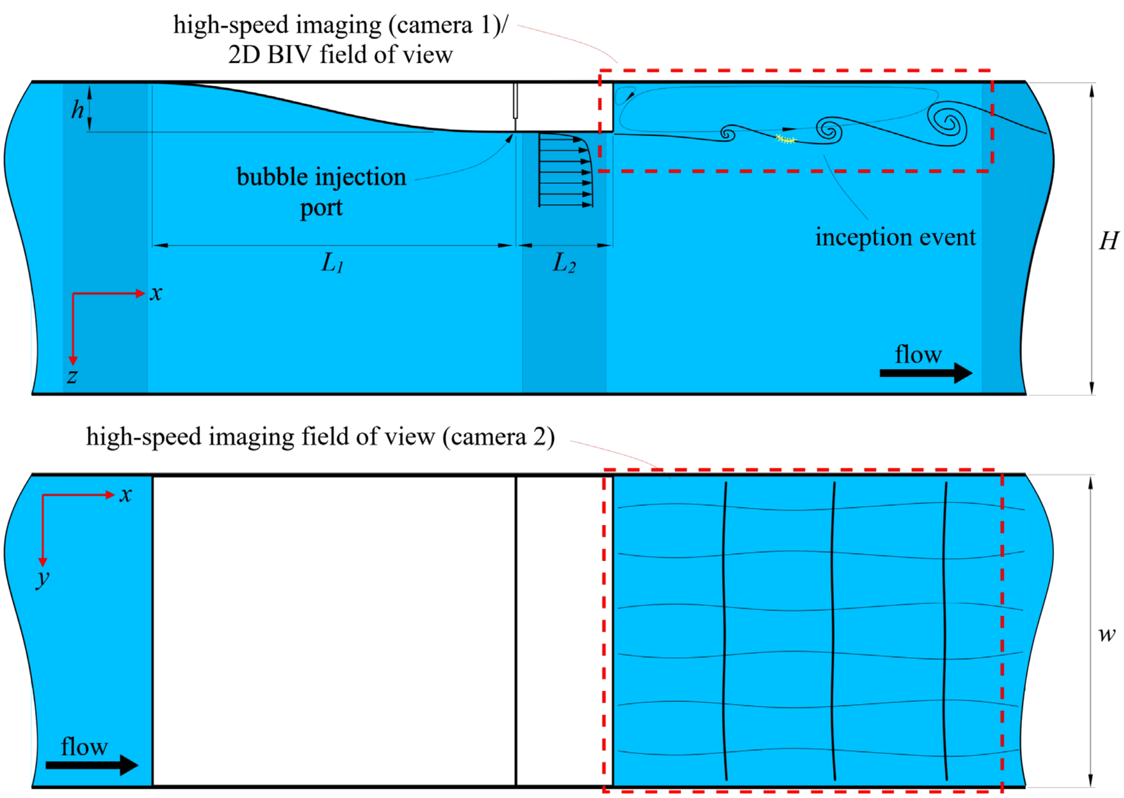

FIG. 2. Schematic of the backward-facing step model used to study cavitation inception in turbulent shear layers. Side view is shown in the top of the figure, and bottom view, below. The origin of the coordinate system is located at the step/ceiling junction.

the stem was removed. The procedure for measurement calibration and data collapse is similar to that described by Belle *et al.* (2016).

Bubble Image Velocimetry (BIV) measurements were performed using microbubble tracers generated by the cavitation of supersaturated water in a confined radial jet (Barbaca *et al.*, 2021). The microbubbles were smaller than 20 μm, with nominal zero-buoyancy ensuring their faithful advection with the flow. The illumination was provided using a CNI MLL-N 532 nm 3 W continuous wave laser, expanded into an $\approx$1 mm thick sheet using a double-concave lens. The flow was imaged with a Phantom v2640 high-speed camera placed to the side of the tunnel test section to acquire images in a x–z plane (Fig. 2). The captured resolution was 2048×1024 pixels, and using a Nikon AF Nikkor 24 mm f/2.8D lens, the resulting magnification factor was 2.54 px/mm. For each measurement, 6000 image pairs were acquired at 100 Hz with a time step dependent on the mean tunnel velocity. The images were cross-correlated using LaVision DaVis 10.0 software with an initial square interrogation window size of 64 pixels with 50% overlap, followed by two passes with 32 pixel windows and 75% overlap. Additional details and validation of the BIV technique are given in Zarruk *et al.* (2014).

High-resolution still images were taken using a Nikon D850 SLR camera with a Nikon AF Nikkor 24 mm f/2.8D lens. The exposure for forward-lit still images was controlled using a triggered stroboscopic flash (Drello 3018/LE4040). The illumination for long-exposure images of cavitation intensity at the test section centerline was the same as that used for the BIV measurements.

High-speed imaging of cavitation inception events was acquired using two simultaneously triggered Phantom v2640 cameras mounted to the side and the bottom of the test section. The side camera was equipped with a Nikon AF Nikkor 24 mm f/2.8D lens, and the images were acquired at a cropped resolution of 2048×800 pixels giving a field of view of $\approx 930 \times 360$ mm^2 at the tunnel centerline. The bottom camera was equipped with a Nikon AF Nikkor 35 mm f/2D lens at full resolution of 2048×1952 pixels with resulting field of view at the tunnel ceiling covering the full span of the test section and $\approx$780 mm in the streamwise direction. Back-lighting was provided by an Effilux EFFI-BL-LITE-1M12P 650×650 mm^2 LED panel, covering the full area of the test section side window. The image acquisition was controlled via Phantom PCC 3.4.4 software with the external triggering signal provided from a BNC Model 575 delay/pulse generator with a 250 ps accuracy. The images were acquired at 6600 and 12 000 frames per second.

Acoustic measurements were obtained simultaneously with high-speed imaging using a Bruel & Kjær Type 8103 hydrophone (voltage sensitivity 25.1 μV/Pa). The hydrophone was mounted in a flooded cavity (kept at the same pressure as the tunnel test section) beneath a 10 mm polyurethane diaphragm, with a 149 mm sensing diameter (Doolan *et al.*, 2013). The hydrophone was mounted in the sidewall at the test section mid-height, approximately 11h upstream of the step. The signal was conditioned with a Bruel & Kjær Nexus conditioner and amplifier, which was also used to apply a 0.1 Hz–100 kHz band-pass filter. The filtered signal was acquired using a National Instruments PXIe-4497 card at a sampling rate of 204.8 kHz.

The experiments for natural nuclei population were performed for a range of step-height based Reynolds numbers, $0.4 \times 10^6 \leq Re = Uh/\nu \leq 1.4 \times 10^6$, where U is the velocity at the streamwise location of the step exit and ν is the kinematic viscosity of the water. The variation in water temperature, and consequently ν, was continually monitored during testing, with the tunnel control system programed to keep a constant Re by adjusting the test-section velocity. The experiments with artificial monodisperse nuclei seeding were performed for $Re = 1.2 \times 10^6$ only. The cavitation number is defined as $\sigma = (p - p_v)/0.5\rho U^2$, where p is the static pressure at the tunnel centerline at the streamwise location of the step tip, p_v is the vapor pressure, and ρ is the water density. Due to the effect of flow contraction induced by the presence of the step, both p and U differ from the tunnel static pressure (p_t) and velocity (U_t) measured at the test section entrance. Therefore, a correction based on the measurement of the pressure coefficient between the test section entrance and the streamwise position of the step tip (C_p) was applied, giving the equations based on the measured tunnel parameters, and derived using Bernoulli's principle, for Reynolds number, $Re = Re_t/\sqrt{1 + C_p}$, and cavitation number, $\sigma = \sigma_t(1 + C_p) + C_p$. Variation in tunnel velocity associated with the changes in Reynolds number resulted with variation in the flow Froude number, $Fr = U/\sqrt{gh}$, where g is gravitational acceleration. Due to the fact that within the present study the focus was on incipient cavities and not on large-scale cavitation, the effect of variation in Fr was considered negligible.

The first set of experiments was performed for a tunnel background, i.e., naturally occurring nuclei population. This population was characterized by Venning *et al.* (2018) using measurements acquired via mechanical activations in a cavitation susceptibility meter (CSM), and a typical nuclei size distribution is presented in Fig. 3. Khoo *et al.* (2020b) showed that this population is practically invariant to tunnel operating conditions and can be taken as a constant. The experiments were performed with a dissolved O_2 content of $\approx$3 ppm.

The second set of experiments was performed with the tunnel water artificially seeded with monodisperse nuclei through a single point on the BFS model. A detailed description of the nuclei injection and measurement method are presented in Sec. V.

III. SINGLE-PHASE FLOW TOPOLOGY

Boundary layer profiles at the nominal position of the step tip were measured at five Re values. The results are shown in Fig. 4 scaled using inner variables and are compared with the law of the wall,

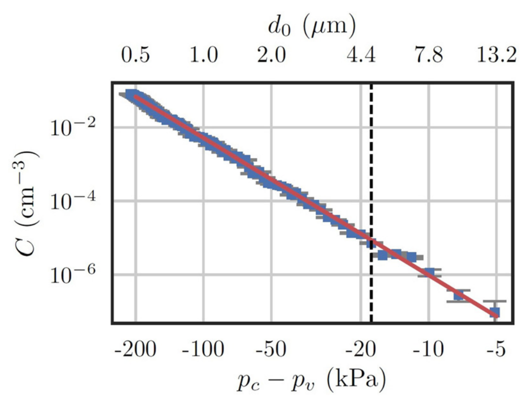

FIG. 3. A typical microbubble population presented as cumulative concentration as a function of the nucleus strength ($p_c - p_v$). This measurement was acquired via mechanical activation in a Cavitation Susceptibility Meter (CSM). The secondary horizontal axis shows the nucleus size assuming spherical bubble dynamics.

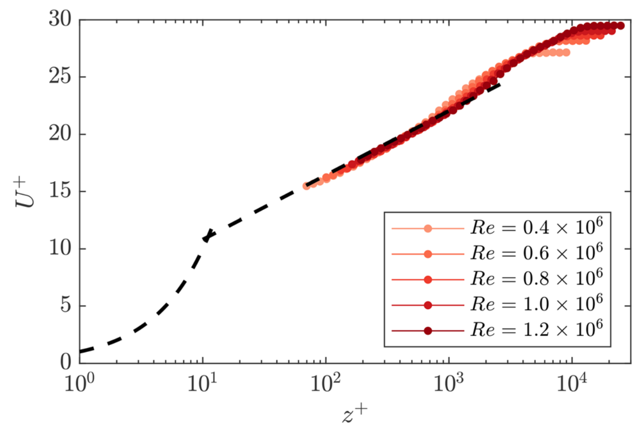

FIG. 4. Comparison of inner-scaled boundary layer profiles with the law of the wall at the nominal step tip position for the range of *Re* investigated.

$U^+ = \frac{1}{\kappa} \ln z^+ + A$, where $U^+ = U/U_\tau$, $z^+ = zU_\tau/\nu$, with U_τ calculated using the method from Belle *et al.* (2016). It can be seen that due to the presence of the step, the boundary layer profiles are modified compared to typical flat-plate boundary layer law of the wall. The modified profiles show a negative defect in the log region, and a positive defect approaching the wake. Boundary layer profiles were found to be consistent across the range of examined *Re*, with a boundary layer thickness of $0.27h$ measured for all cases.

Streamlines of the ensemble-averaged velocity vector fields downstream of the step obtained using BIV for $Re = 1.2 \times 10^6$ are presented in Fig. 5. The spatial coordinates are scaled by h, and the step position is indicated by the gray box in the upper left corner. The illumination and bubble seeding were optimized for measurement of the re-circulation zone length, and consequently resulted with noisy streamlines within the re-circulation up to $2h$ downstream from the step. The white area on the left side of the image represents the region where illumination was not sufficient to obtain a rigorous measurement. The velocity field topology was found to be independent of *Re*, and the streamlines show the typical re-circulation zone characteristic for the separated flow in the wake of the step. The ensemble-averaged length of the re-circulation zone ($\bar{x}_r$) is unaffected by variation in *Re*, with $\bar{x}_r$ value of $6h$. The variation in $\bar{x}_r$ was less than 1% across the range of examined *Re*.

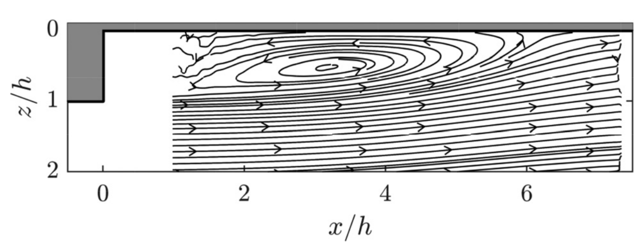

FIG. 5. Typical example of streamlines of ensemble-averaged velocity vector fields obtained using bubble image velocimetry, showing the re-circulation zone in the wake of the step. The particular example is for $Re = 1.2 \times 10^6$. The step is indicated with a gray box in the upper left corner.

IV. CAVITATION INCEPTION FOR NATURAL NUCLEI FLOW

Forward-lit high-resolution still images depicting the cavitation topology for a range of cavitation numbers (controlled via the tunnel test-section pressure), $0.65 \geq \sigma \geq 0.4$ for a constant $Re = 1 \times 10^6$ are presented in Fig. 6. The outline and the position of the step in the upper left corner of the images are indicated with a gray box. At $\sigma = 0.65$, cavitation activity is almost negligible, with only occasional appearance of incipient cavitating structures. Incipient cavities appear more regularly as σ is decreased to 0.6. With further decrease in σ, the number and extent of the cavitating structures increases and the structures expand within the cores of the QSVs characteristic of the shear layer flow.

As σ is decreased below 0.5, the cavitation topology starts to resemble that of developed shear layer cavitation. Across the range of investigated σ values, no cavitation in the larger spanwise vortices is observed, which is in agreement with the observations of shear layer cavitation at lower *Re* values from the literature. The increase in cavitation activity with decreasing σ results in the generation of a large quantity of microbubbles during the collapse of cavitating structures. These microbubbles are ingested into the re-circulation zone in the wake of the step, as is particularly noticeable at $\sigma = 0.4$, as a fine microbubble cloud. The generation of the microbubbles and their influence on the cavitation inception and extent will be discussed further on in the text. The observations of cavitation topology presented in Fig. 6 are pertinent for all *Re* investigated.

The spatial distribution of the intensity of shear layer cavitation in the wake of the BFS is examined using long-exposure photography. A 1 mm thick vertical plane at the test section centerline was isolated using laser sheet illumination. Cavitation intensity maps are obtained from 300 s exposures, with background elimination via an image acquired at the same exposure settings for non-cavitating conditions. The maps obtained for a range of *Re* and σ investigated are presented in Fig. 7.

Similar to the observations from still imaging, very little cavitation activity can be observed at $\sigma = 0.65$. Irrespective of *Re* value, an increase in cavitation intensity is seen with decreasing σ. At the lower σ values, an area of higher light intensity streaks just downstream of the step is present. This area is an artifact of the light scattered off the increasing number of remnant microbubbles trapped in the re-circulation zone (as observed in Fig. 6), and it is not representative of cavitation intensity. An increase in cavitation intensity is observed with increasing *Re* at σ values below 0.6, i.e., for conditions where inception events occur regularly. The effect of variation in *Re* on cavitation intensity is much less than that of variation in σ. For the condition where σ is above 0.6, i.e., where inception occurs irregularly, an increase in cavitation intensity can be seen for the lowest *Re* value; however, at the higher *Re*, the trend is consistent with that observed at lower σ.

The position of the main peak in cavitation intensity is found $3-4h$ downstream of the step tip and about $0.75h$ from the tunnel ceiling. The position of the main peak is found to be mostly unaffected by the variation in either *Re* or σ.

Agarwal *et al.* (2018), for a geometrically similar flow, present maps depicting the spatial probability of incipient cavities obtained using high-speed imaging for *Re* values an order of magnitude lower than the *Re* values in the present study. The resulting maps, although

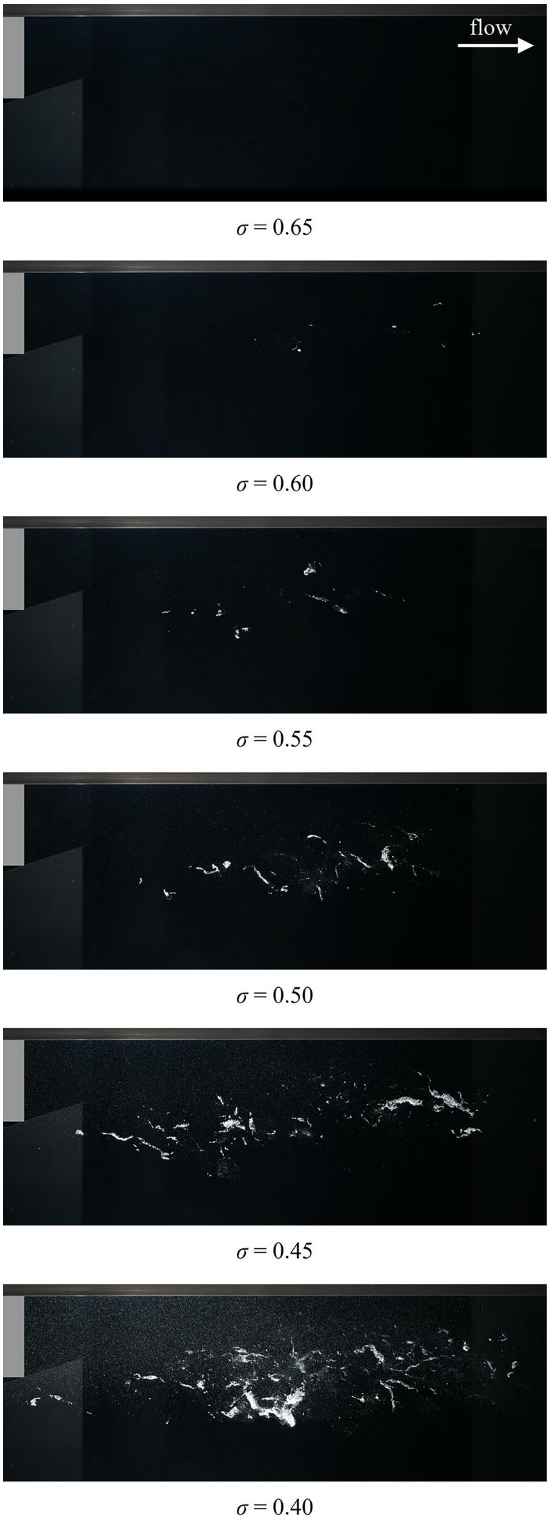

FIG. 6. Forward-lit still images showing the cavitation topology for the range of cavitation numbers, $0.65 \geq \sigma \geq 0.4$, and $Re = 1 \times 10^6$. The step position in the upper left corner of the images is indicated with a gray box.

obtained with different methods, compare favorably. It can be noted that in their smaller scale experiment, Agarwal *et al.* (2018) report a $0.1x_r$ shift in the position of the intensity peak upstream toward the step as *Re* increases. This was not observed in the present higher *Re* experiment, which suggests that the position of the cavitation intensity peak becomes independent of *Re* at high *Re* values.

To provide more quantitative evaluation of the cavitation intensity, horizontal and vertical line-plots were extracted from the two-dimensional maps at the position of the intensity peak, i.e., horizontal plot at $y = 0.75h$ and vertical plot at $x = 3.5h$. These plots for the range of examined *Re* and $\sigma = 0.5$ are shown in Figs. 8(a) and 8(b). Similarly, the plots for the range of examined σ and $Re = 1 \times 10^6$ are shown in Figs. 8(c) and 8(d). The main observation from these plots is that the increase in the value of the main cavitation intensity peak is six times larger across the range of investigated σ than it is across the range of investigated *Re*, emphasizing σ as the dominant flow variable. It can be seen that the intensity, both in the horizontal and vertical line-plots, has a broad peak at higher σ, which becomes more defined as σ is decreased. Additionally, the inception events are observed across a wider area (increased width of higher cavitation intensity in the line-plots) in both directions as σ decreases, while the area susceptible to inception events remains largely unaffected by variation in *Re*.

The topology and evolution of discrete incipient cavities is examined using back-lit high-speed imaging. Cavitation inception occurred in the QSVs characteristic of the underlying shear layer flow. Incipient cavities are observed to develop into either "spherical" or stretched vortical structures, across a wide range of sizes, ranging from less than 1 mm to over 100 mm in diameter/length (Fig. 9). The appearance of spherical structures is mostly opaque with a rough/broken surface, while the stretched vortical structures are more transparent with a smoother surface. Larger stretched structures form a continuous cavity within a vortex core, such as that shown in Fig. 9(d). The smaller stretched vortices appeared as discrete structures or as a series of non-continuous structures activated within a single vortex core.

A sequence of extracted frames from the back-lit high-speed videos depicting evolution of a discrete incipient cavity is shown in Fig. 10. A nucleus is activated in (a) near the left edge of the frame and the inception time is defined as 0 ms. The incipient cavity rapidly expands into a large opaque spherical structure (b) within 1.58 ms. This structure breaks into a pair of smaller structures under the influence of the shear layer turbulence (c). These smaller structures eventually collapse/condense emitting shock-waves (d), as discussed in more detail by Barbaca *et al.* (2019). While the condensation shock-waves were identified in the high-speed imaging, their intensity is not sufficient to impart signature in the acoustic measurements. The whole process from inception through to the first collapse lasts only 3.75 ms. During the condensation of a structure, a population of microbubble products is generated, forming a cloud of remnant microbubbles (e). These remnant microbubble populations have characteristics similar to those of the populations in the wake of a cavitating object at high *Re*, as presented in Fig. 1. Due to their larger size and increased concentration compared to those of the natural nuclei population, they act as preferential sites for new inception events to occur. As can be seen in (f), a number of remnant microbubbles contained within a cloud are reactivated forming new incipient structures. These structures go through a similar process as the initial structure, depicted in (a)–(e), which results in the formation of an even denser population of

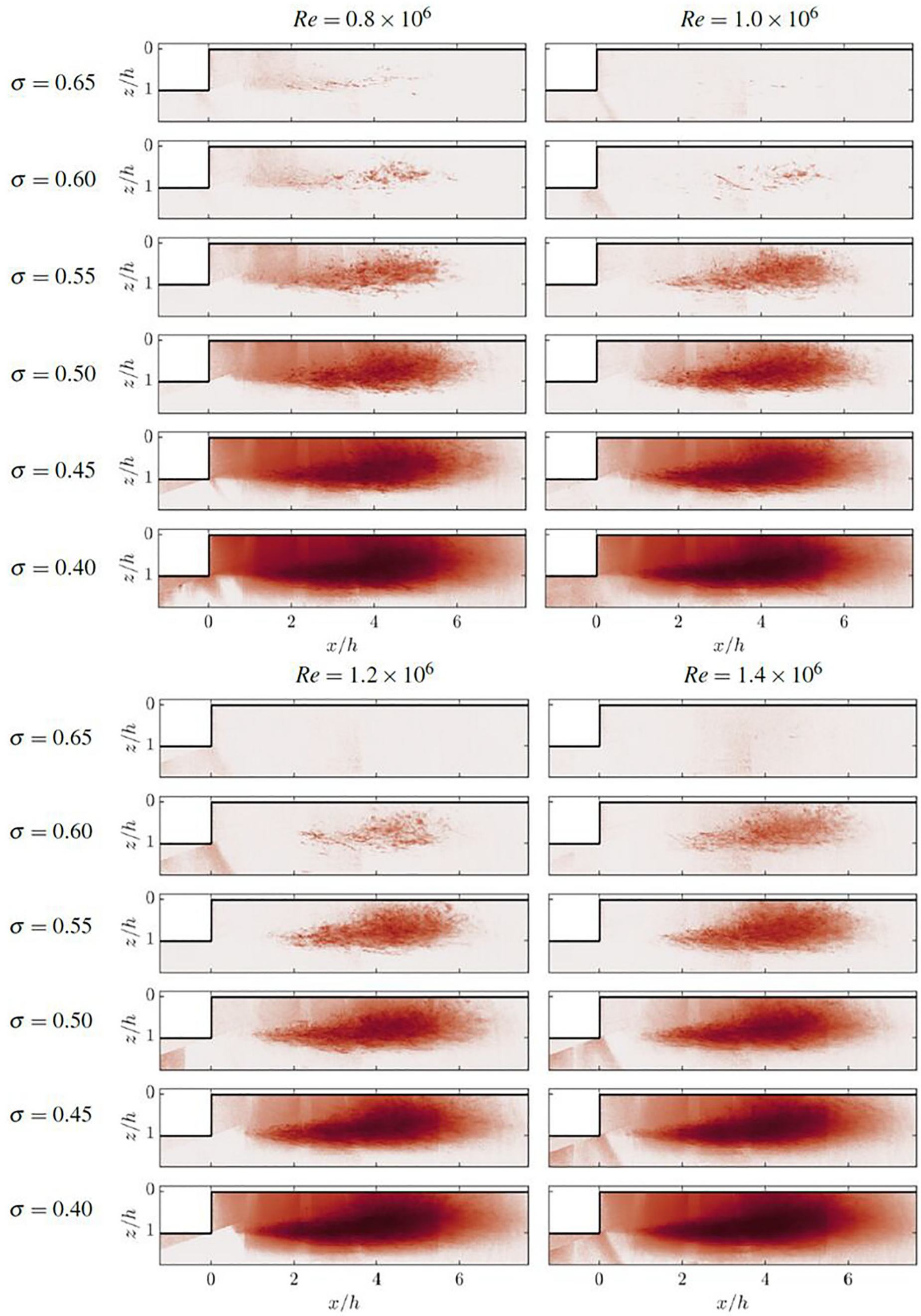

FIG. 7. Spatial distribution maps of the cavitation intensity across the range of *Re* and σ investigated, obtained from a 5 min long-exposure still photography. Laser sheet illumination was used to isolate a 1 mm thick *x*–*z* plane at the test section centerline. The step is indicated by a white box in the upper left corner. The flow is from the left to right.

remnant microbubbles over a larger volume. The repetition of the inception/collapse process triggers a compounding effect on the number of activations, thus initiating developed shear layer cavitation. The structures formed through this process do not necessarily form the same type of cavities as the initial structure, as it can be seen in (g) where a stretched vortical structure was incepted from the remnants of a collapsed spherical structure. The remnant microbubble cloud is eventually advected downstream of the camera field of view.

As described above, the microbubble cloud population is dispersed into the shear layer vortices downstream of the initial event triggering more shear layer cavitation events as it is advected. Furthermore, the microbubbles can also be entrained into the recirculation zone in the wake of the step, where they remain trapped for a prolonged period of time. These trapped microbubbles are occasionally ejected into the shear layer where they act as preferential nuclei, maintaining developed shear layer cavitation for substantially

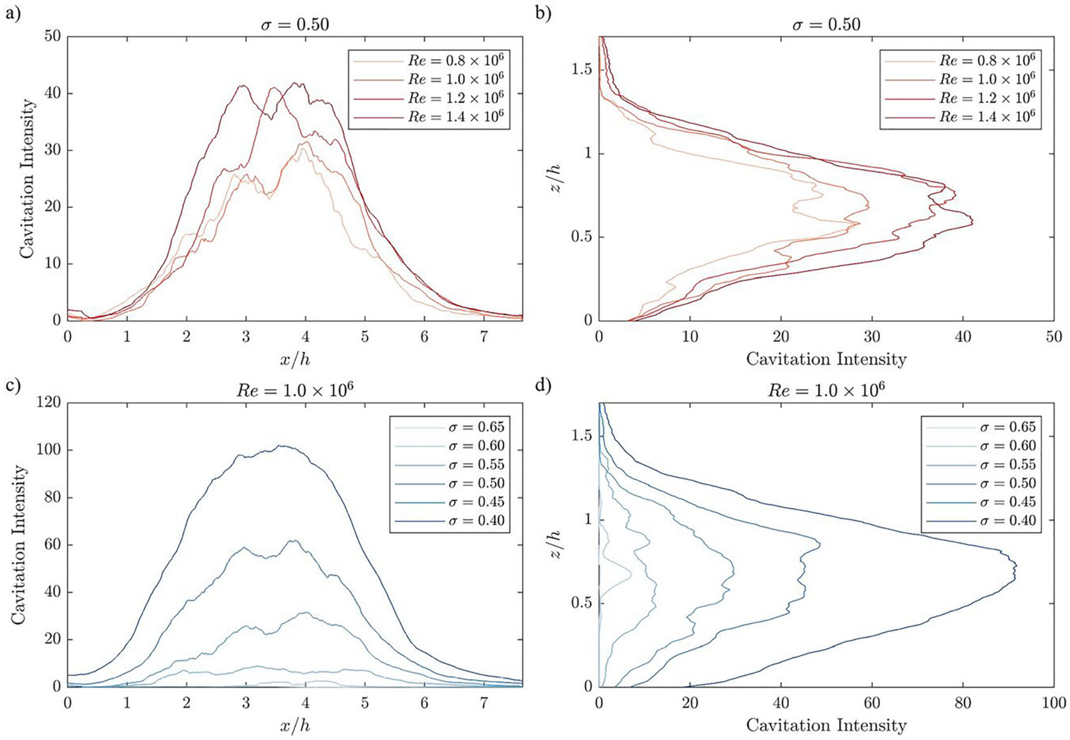

FIG. 8. Line-plots representing horizontal and vertical slices of the cavitation intensity maps for $z = 0.75h$ (a) and (c) and $x = 3.5h$ (b) and (d), respectively. The plots in (a) and (b) are for the range of examined Re and for constant $\sigma = 0.5$. The plots in (c) and (d) are for the range of examined σ and for constant $Re = 1 \times 10^6$.

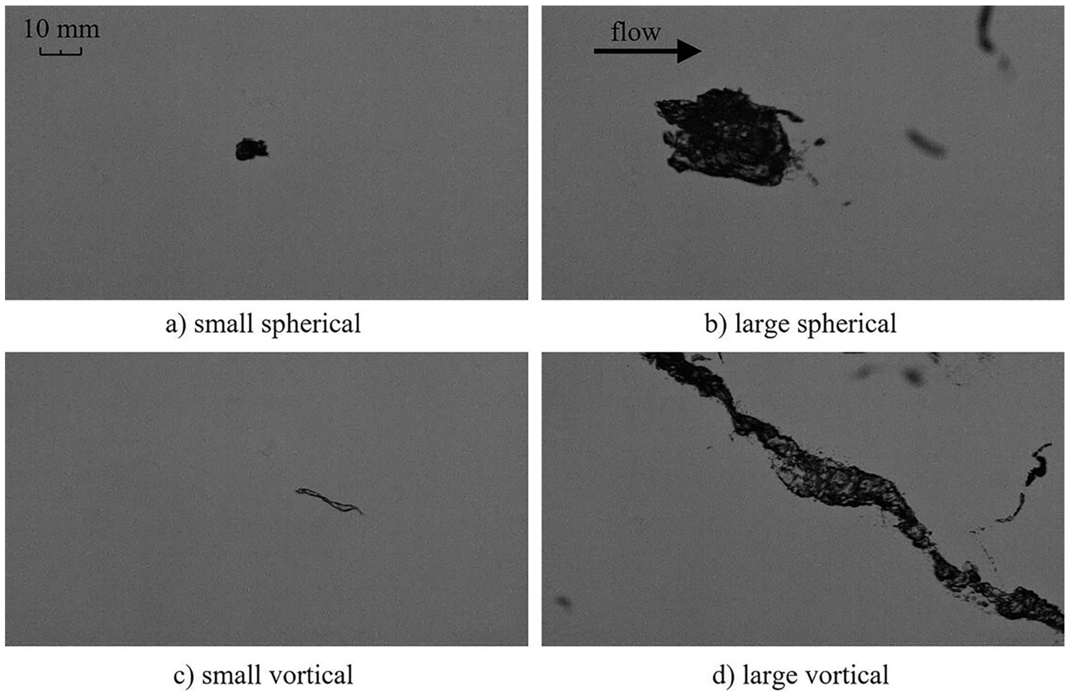

FIG. 9. Extracted images from high-speed videos showing the two main types of cavitating structures: spherical and vortical structures, and an indication of the cavitating structures' size range.

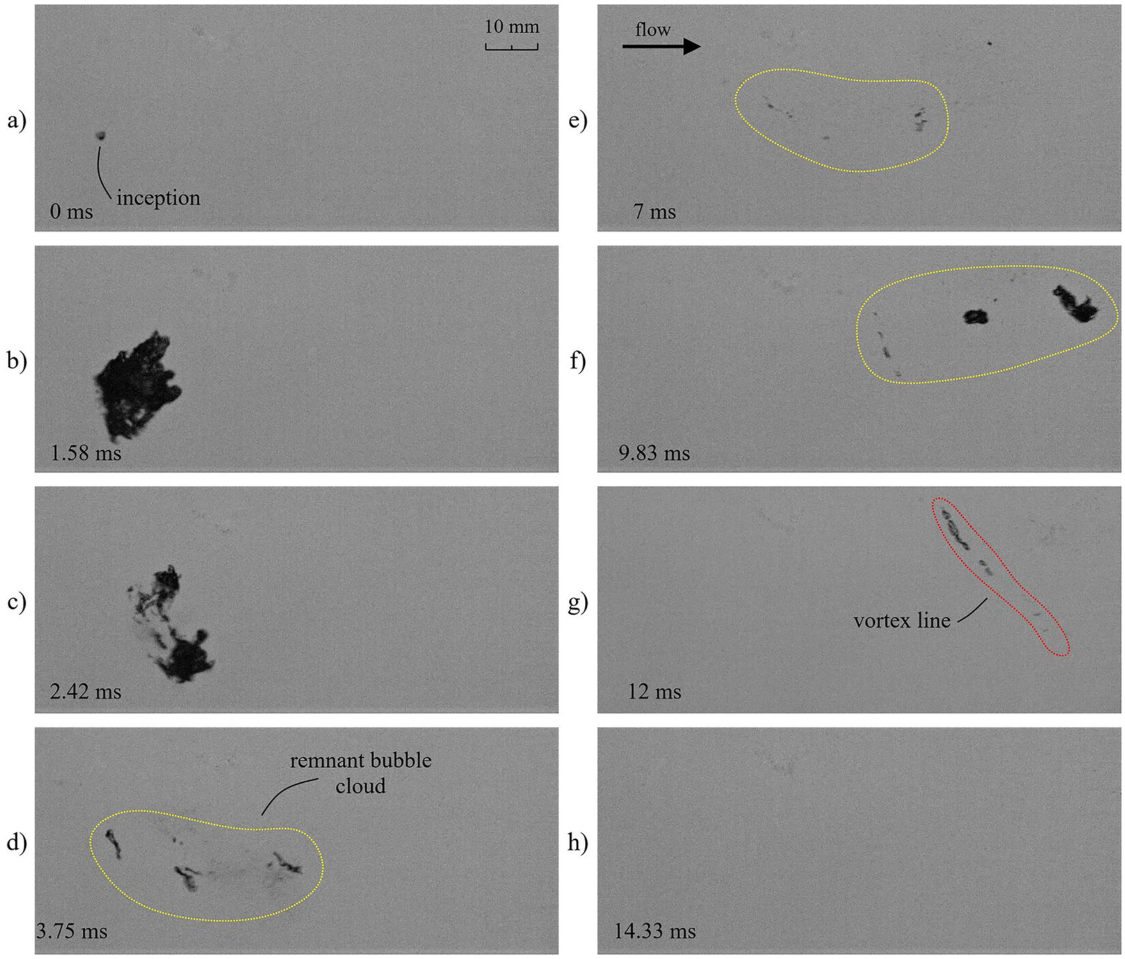

FIG. 10. Sequence of images extracted form high-speed videos showing the evolution of a discrete incipient cavity. Inception occurs in (a), followed by growth of a spherical structure (b), breakup, (c) and collapse (d). The remnant bubble cloud generated during the structure collapse can be seen in (e), and is responsible for flow re-nucleation and formation of new spherical structures (f). This process repeats again resulting with formation of a vortical structure (g). The remnant bubble population is advected downstream by the flow (h). The sequence was recorded for $Re = 1 \times 10^6$ and $\sigma = 0.6$. The center of the imaged area is located $4h$ downstream of the step and $0.75h$ below the test section ceiling.

longer periods, often requiring σ to be increased well above the incipient value for developed cavitation to disappear. From these observations, it can be concluded that once a discrete inception event occurs, it almost invariably, through the process of re-nucleation, triggers sustained cavitation activity if the flow conditions are maintained.

The effects of re-nucleation manifest as a hysteresis between the incipient and desinent cavitation numbers. In Fig. 11, a plot of the sound pressure levels against σ is presented for $Re = 1 \times 10^6$. The plot is obtained by transiently reducing σ in a non-equilibrium state until cavitation inception occurs, which is marked as the incipient cavitation number σ_i. Afterward, σ is increased following the same procedure until the cavitation completely disappears, marking a desinent cavitation number σ_d. It can be seen that cavitation inception triggers a large and abrupt increase in the sound pressure level. While the inception causes an abrupt change, the decrease in sound pressure with increasing σ is gradual, with cavitation activity persisting at σ values higher than σ_i. As σ_d is reached, the sound pressure level decreases to the same level as that measured before the cavitation started.

The blue circles represent the sound pressure values from steady-state measurements, i.e., the values acquired after a particular σ value was held constant for 10 min. The blue circles correspond well with the values recorded while increasing σ in the non-equilibrium state, suggesting that the σ_i value is dependent on the measurement period. This dependence stems from the fact that as the measurement period is increased, there is a higher chance for large nuclei to be dispersed into the shear layer. These observations are similar to those observed for tip vortex cavitation by Khoo *et al.* (2020a), and further emphasize the importance of precise control and characterization of the water nuclei content during inception experiments.

Variability in σ_i and σ_d is investigated by performing ten consecutive hysteresis measurements for three Re values, as shown in Fig. 12. Each hysteresis measurement is recorded after 120 s at non-cavitating flow conditions. It can be observed that σ_i varies significantly, as it is dependent on the stochastic variation in the availability of large nuclei. The desinent cavitation number is more consistent as desinence occurs when the minimum pressure in the secondary vortices increases above

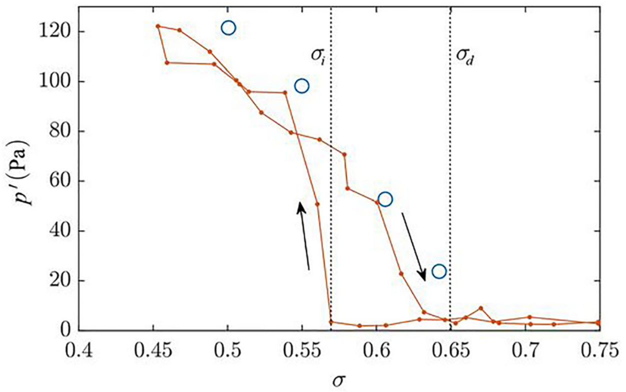

FIG. 11. Plot of sound pressure level obtained by reducing and increasing σ in non-equilibrium state, showing the hysteresis between the incipient and desinent cavitation number. Blue circles represent the equilibrium state measurements. Measurements are for $Re = 1 \times 10^6$.

vapor pressure, removing the dependence on nuclei content. It is also observed that the magnitude of variability of σ_i increases with a decrease in *Re*, from about 0.1 at $Re = 1.4 \times 10^6$ to about 0.2 for $Re = 1 \times 10^6$. Greater consistency in σ_i values seen at the higher *Re* originates from increased availability of large nuclei susceptible to cavitation per unit time due to the larger volume of water entrained into the shear layers at higher *Re*. Although, both Russell *et al.* (2018) and Barbaca *et al.* (2019) observed decrease in the size of microbubbles generated by cavitation with increasing *Re*, the increase in the overall availability of nuclei appears to be sufficient to ensure greater consistency of σ_i at higher *Re* values.

The effect of hysteresis, coupled with the stochastic nature of both the pressure in the core of QSVs and the natural nuclei population, made characterization of the discrete inception events challenging. Based on this, it can be concluded that re-nucleation is a dominant feature controlling cavitation inception in the examined flow, which masks the physics of the discrete inception events for tests performed with the natural nuclei population. In order to avoid hysteresis and formation of developed shear layer cavitation, an approach

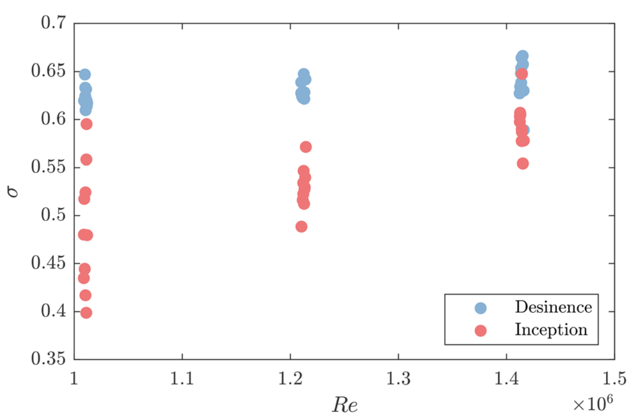

FIG. 12. Range of incipient and desinent cavitation numbers obtained from ten non-equilibrium measurements at three *Re* values.

utilizing injection of a monodisperse microbubble population with the nuclei critical pressure close to vapor pressure may be advantageous.

V. MONODISPERSE NUCLEI INJECTION AND MEASUREMENTS

The equilibrium of a microbubble (nuclei) becomes unstable if the flow local pressure is reduced below a critical value, p_c. If the local pressure value remains below p_c for a sufficient time period, the nuclei becomes activated (undergoes explosive growth) and is classified as a site of a cavitation inception event. Nuclei critical pressure is dependent on the nuclei initial size (d_0) and ambient pressure (p_∞) as per the following equation:

$$p_c = p_v - \sqrt{\frac{4}{27\left[\left(\frac{d_0}{4S}\right)^3 (p_\infty - p_v) + \left(\frac{d_0}{4S}\right)^2\right]}}, \qquad (1)$$

where p_v is the water vapor pressure, and S is the surface tension. This equation can be derived from consideration of the equilibrium of bubble internal and external pressures and the surface tension assuming isothermal internal gas behavior and no mass transfer via phase change or diffusion (Franc and Michel, 2004).

The natural nuclei population in the AMC water tunnel has been previously characterized using a Cavitation Susceptibility Meter (CSM) measurements (Khoo *et al.*, 2020b; Venning *et al.*, 2018), as presented in Fig. 3. Measured cumulative size distribution was found to follow a power law like decrease in nuclei concentration with increase in nuclei size, with the largest measured nuclei of the order of 10 μm in diameter. From Eq. (1), it can be calculated that for the largest nuclei contained within the natural population, the critical pressure is $\approx$5.5 kPa below p_v or $\approx$2.5 kPa below zero, i.e., for the natural nuclei to get activated, the water must be in tension. As the natural nuclei follow a power law, the largest nuclei are, however, present in extremely small concentrations.

As previously discussed, the stochastic nature of the water nuclei content can be reduced by artificially seeding the water with a monodisperse nuclei population, where the critical pressure is equal for all nuclei. To ensure that the seeded population is the only active population at a particular cavitation number, p_c for seeded nuclei has to be markedly higher than that for the largest nuclei contained in sufficient concentration within the natural population. To satisfy such a requirement, a capability to seed the flow with monodisperse nuclei $\approx$60 μm in diameter ($p_c \approx p_v$) has been developed at the AMC.

Targeted seeding of a high *Re* flow with a monodisperse population of large nuclei was difficult to achieve. An in-wall nuclei injection system based on the use of a microfluidic T-junction, routinely utilized for the experiments at CRL (Russell *et al.*, 2020b), suffered with issues related to bubble breakup. High velocity gradients and shear between the flow delivering the nuclei through the injector port and the freestream flow induced bubble breakup, with products being generated across a wide range of sizes. Given the stochastic size distribution and uncertainty in the total number of bubbles generated by the bubble breakup process, the modified population was deemed neither rigorous nor feasible for use in the current experiment. An injection system with the outlet of the injector tube orientated in the streamwise direction to limit the velocity gradients was trialed; however, this also did not yield a satisfactory result.

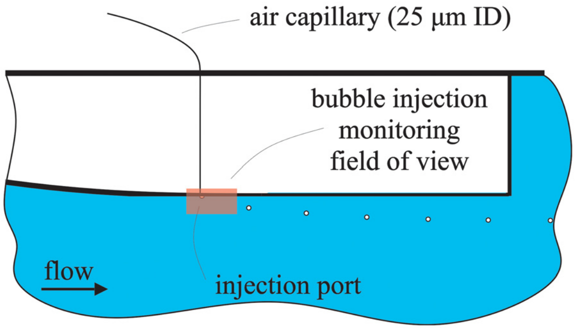

FIG. 13. Schematic of the nuclei injection system consisting of a 25 μm diameter air capillary connected to the injection port flush to the BFS surface. Bubbles are produced via inertial pinch-off of the air volume at the injection port outlet due to the high velocity gradient and shear between the injector and freestream flows.

Following these observations, a different approach, based on the use of the high wall shear at the injection port as a mechanism for bubble generation, was employed. For this purpose, a novel system incorporating an air capillary with the outlet mounted flush to the injection port at the BFS wall has been developed.

A schematic of the system is presented in Fig. 13. Pressurized air is delivered to the injection port via a 358 mm long 25 μm diameter capillary tube, with the supply pressure regulated using a Proportion-Air QPV1TBNISZP10BRGAXL electronic regulator (range 0–10 bar) equipped with a Prevost 1 μm air filter. The growing air volume undergoes coherent pinch-off similar to T-junction microbubble production through a balance of increasing bubble drag, with increasing wall shear overcoming bubble surface tension.

To examine and monitor the bubble generation process at the injection port, high-speed shadowgraphy imaging of the injector port region (indicated with a red box in Fig. 13) was performed. The imaging setup utilized for this purpose consists of a Photron Fastcam SA5 high-speed camera with a maximum resolution of 1024×1024 pixels equipped with a Nikon AF-D 200 mm f/4 macrolens. The images were acquired at a reduced camera resolution of 256×64 pixels at 300 000 frames per second, with illumination provided from a single SciTech Constellation 120 continuous LED lamp. To examine the size distribution of the generated bubbles, a high-speed camera was replaced with a high-resolution camera, IO Industries Flare 48M30 CX high-speed CMOS camera with a resolution of 7920×6004 pixels. To obtain converged bubble size distribution, still images were acquired until 5000 bubbles were detected for each investigated condition. The generation process was examined for a wide range of combinations of tunnel and air capillary pressures, with the pressure ranges from 75 to 175 and 150 to 450 kPa, respectively.

A sample shadowgraphy image of a representative bubble train is shown in Fig. 14. For each combination of pressures, the train consisted of bubbles, with the majority ranging between 50 and 70 μm in diameter (Fig. 15), and the production rate controlled by the differential pressure between the capillary inlet and the tunnel. From Eq. (1), it can be calculated that the variation in critical pressure between size range extremes of the generated population is about 0.2 kPa and, therefore, the population can be considered as near monodisperse. As the critical pressure at the lower end of the generated population size range is still well above the critical pressure of the largest nuclei contained in sufficient concentration within the natural populations, injected nuclei are sufficiently more susceptible to cavitation inception than the natural nuclei. Based on these two considerations, the population generated via shearing within the BFS wall boundary layer is deemed satisfactory for use in the experiment.

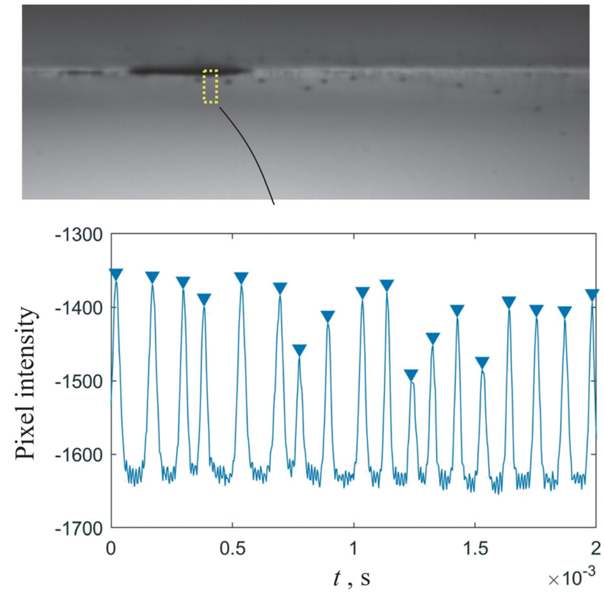

FIG. 14. Sample shadowgraph image of the bubble train at the outlet of a capillary tube mounted flush to the backward-facing step wall. Bubbles are produced by fragmentation of the air volume by the high shear within the step wall boundary layer. A 3×11 pixels subsample, marked with a yellow box, is used for the analysis of the bubble production rate. A 0.002 s time series of the inverted sum of the pixel intensity of the subsample is shown below the image, with the marked peaks denoting the passage of a bubble.

A 3×11 pixel subsample of the image positioned just downstream of the air capillary outlet, noted with a yellow box in Fig. 14, was used for the analysis of the bubble production rate. A time series

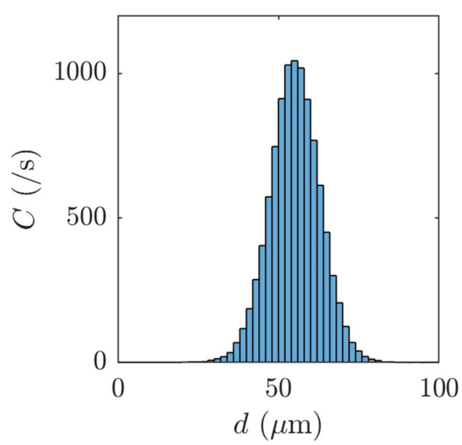

FIG. 15. Typical size distribution of the bubbles generated by the nuclei injection system across all operating points.

of the inverted value of the sum of the pixel intensity across the subsample is shown at the bottom of Fig. 14. Each time series was analyzed using a peak finding algorithm, with the passage of each bubble (shadow in the image) marked with a peak in the inverted intensity.

The bubble production rate dependence on the differential pressure between the capillary inlet and the tunnel was analyzed for a tunnel pressure $p = 80$ kPa and capillary pressure range $150 \leq p_{air} \leq 450$ kPa, varied in 50 kPa increments. A sample containing 50 000 frames was acquired for each condition. Dependence of the bubble production rate, f_b, on the pressure differential between the air capillary inlet and the tunnel, $\Delta p = p_{air} - p$, is presented in Fig. 16. The injection system is capable of producing bubbles at a rate of the order of 10 kHz, f_b increasing linearly with an increase in Δp at a rate of about 57 Hz/kPa. A linear fit function through the data points is represented with a dashed line in Fig. 16. For the purposes of the current study, an operating point with $f_b \approx 11$ kHz is selected.

The time series of the subsample pixel intensity indicates that the bubble production rate is not perfectly consistent across the acquired sample, with instantaneous variations in bubble production of about ± 200 Hz. However, the time scale of the variations are much shorter than the acquisition periods of nuclei and cavitation inception measurements, and consequently, these are unaffected by this small variation in the bubble production rate.

A more detailed description of the presented bubble generation method, including theoretical foundations and a systematic study of the effect of variation in the capillary geometry and flow parameters will be a topic of a separate study to be reported in the near future.

While seeding the flow with near monodisperse nuclei addresses one aspect of the stochastic nature of nuclei content, the spatial distribution of nuclei within the flow still remains a stochastic variable. In order to statistically characterize the spatial distribution of the injected nuclei plume, a volumetric nuclei measurement technique based on use of Mie-Scattering Imaging (MSI) has been developed.

A schematic representation of the experimental setup used for spatial characterization of the nuclei plume is shown in Fig. 17.

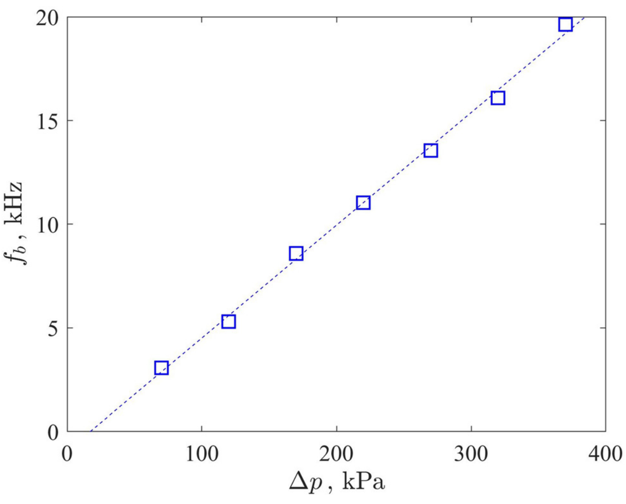

FIG. 16. Dependence of bubble production rate (f_b) on the differential pressure between the air capillary inlet and the tunnel (Δp), with $p = 80$ kPa. Linear fit through the data points is denoted with a dashed line.

The MSI measurements were acquired using a 48MP IO Industries Flare 48M30 CX high-speed CMOS camera equipped with a Nikon AF-S Nikkor 85 mm f/1.4 lens, located to the side of the test section. Bubbles were illuminated using an Ekspla NL204-SH TEM_{00} laser emitting 532 nm light with pulse frequency of up to 1 kHz and energy of 2 mJ per pulse. The laser was mounted horizontally below the tunnel test section, with the beam directed into the tunnel using two Thorlabs NB 1-K12 1″ Nd:YAG mirrors. The beam entered the tunnel test section through a 80 mm thick acrylic window. To prevent burning of the acrylic window, the laser had to be operated at the lower power output, limiting the lower bound of detectable bubble size range. The beam was angled 7° from the vertical axis to prevent any reflected and refracted rays from overlapping the measurement beam. Accordingly, the camera was rotated so that the horizontal axis was parallel to the direction of the beam propagation. The camera was set with the sensor plane normal perpendicular to the beam so that the measurement angle was 90°.

Spatial characterization is achieved by jointly traversing the laser beam and the camera across the wake of the BFS. Position of the laser beam is adjusted by traversing the location of the two mirrors directing the beam into the tunnel. Streamwise positioning is achieved by mounting both mirrors on an Isel linear traverse with a 600 mm travel. Mechanical considerations limit measurements to the range of positions from the step-up to 500 mm downstream. Spanwise positioning is achieved by mounting the mirror M2 on a Zaber linear traverse with a 200 mm travel attached to the streamwise traverse, enabling measurements 100 mm each side of the tunnel centerline. To maintain the camera streamwise position coincident with the position of the laser beam, as well as the camera defocused distance, the camera was mounted to an identical traverse setup as the mirrors directing the beam.

Measurements of the nuclei spatial distribution were performed for three streamwise (x–z) and five spanwise (y–z) planes. Streamwise planes included the tunnel center plane ($y = 0$) and planes located at $y = 0.2$ and $0.4h$. The increment between measurement points in the streamwise direction was set to $0.2h$. Spanwise distributions were obtained at the locations $x = 1,\ 2,\ 3,\ 4,$ and $5h$ downstream of the step. Increment between measurement points in the spanwise direction was set to $0.2h$. As the laser beam is nominally aligned with the vertical axis, vertical distribution is obtained along a continuous line, i.e., did not require incrementation. Due to symmetry of the bubble plume, only one side of the plume was captured for both the streamwise and spanwise distributions.

The plume was characterized for the same flow *Re* as cavitation inception, but at a non-cavitating σ value (≈ 4) to ensure that bubble population is not modified by cavitation products. For each measurement position, images were acquired until a statistically significant number of bubbles was detected (minimum of 500 bubble detections). The required number of images varied depending on the bubble concentration across the plume, and accordingly, samples of between 50 000 and 200 000 images were acquired. Given the sampling rate of 500 Hz, image acquisition for all the planes of interest took ≈ 20 h. The MSI measurement calibration, data processing, and analysis were performed using the method developed by Russell *et al.* (2020a) and (2020b), and, for brevity, only a brief summary will be provided here. A high-speed shadowgraphy dataset of the bubble injection through the injector port was acquired every 10 min to monitor the bubble production rate.

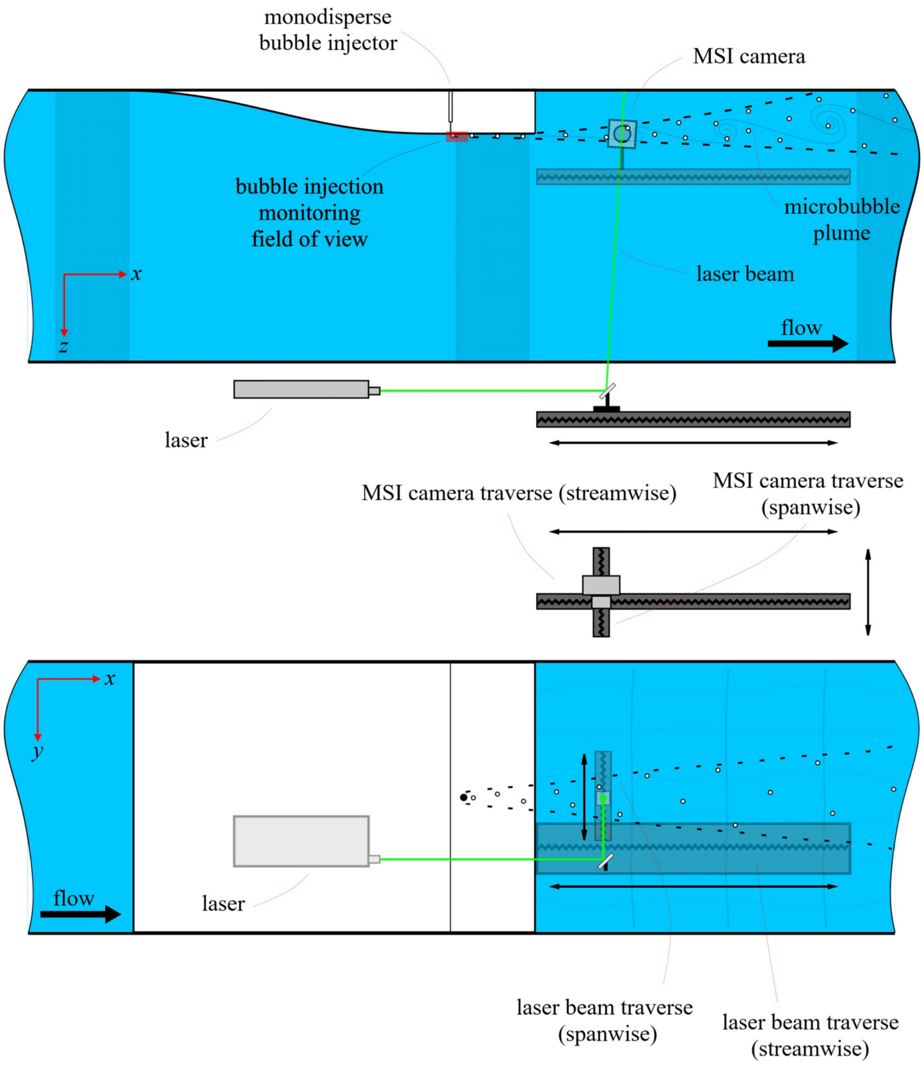

FIG. 17. Schematic of the optical system used for the characterization of spatial distribution of nuclei in the wake of the backward-facing step. Side view is shown in the top, and bottom view, in the bottom of the figure. The area shaded with red in side view represents the field of view of shadowgraphy measurements at the location of the nuclei injection port. The traverse system enables MSI measurements of nuclei in the wake of BFS from the step to 5.5 step heights downstream in the streamwise direction and a step height each side of the tunnel centerline in the spanwise direction.

MSI images were analyzed using a custom MATLAB script. Each interference pattern was reduced to a representative one-dimensional "pixel series" of the same width as the original pattern. To generate these series, an iterative algorithm based on use of cross correlation was used to extract the brightest interference pattern from an image, masking out the circular area afterward. The masked image was then re-processed, and the processing continued until the median of the intensity series extracted in the current step was lower than a specified intensity threshold. As the flow was seeded with near monodisperse nuclei, with the size monitored at the injection point, MSI was not used for sizing and, consequently, a calibration of angular wavelength constant was not performed.

The effective measurement volume for MSI is dependent on bubble size and characteristics of the optical setup. The scattered light intensity of a bubble is nominally dependent on the square of the diameter. Therefore, for a Gaussian beam profile, the scattered light intensity will depend on the bubble size and its location in the beam profile. In this instance, the volumetric calibration was simplified due to use of near monodisperse seeding. For this purpose, all the bubbles were considered to have a 60 μm diameter (median value from Fig. 15), which resulted with an effective laser beam diameter of $\approx$ 1 mm. All the MSI data acquired during this experimental campaign was compiled to obtain the volumetric calibration ($\sim 10^6$ bubble detections).

Contour plots of bubble concentration, C, distribution for the streamwise planes are presented in Fig. 18, and for the spanwise planes, in Fig. 19. Note that due to the wide range of concentration values, color shading is logarithmically distributed. Nuclei are injected at a rate of $f_b = 11$ kHz at a position about 200 mm upstream of the step. The injected plume undergoes limited dispersion within the BFS wall boundary layer as it is advected along the BFS surface. The highest nuclei concentration, $C \approx 1\ \mathrm{ml}^{-1}$, can be observed for the measurement point closest to the step and located at the tunnel $y = 0h$ plane (injector port plane). As nuclei are advected further downstream of the step, formation and increase in size of the shear layer structures promote dispersion of nuclei in the spanwise directions. This results in an increase in the extent of the nuclei plume in the y–z plane, and

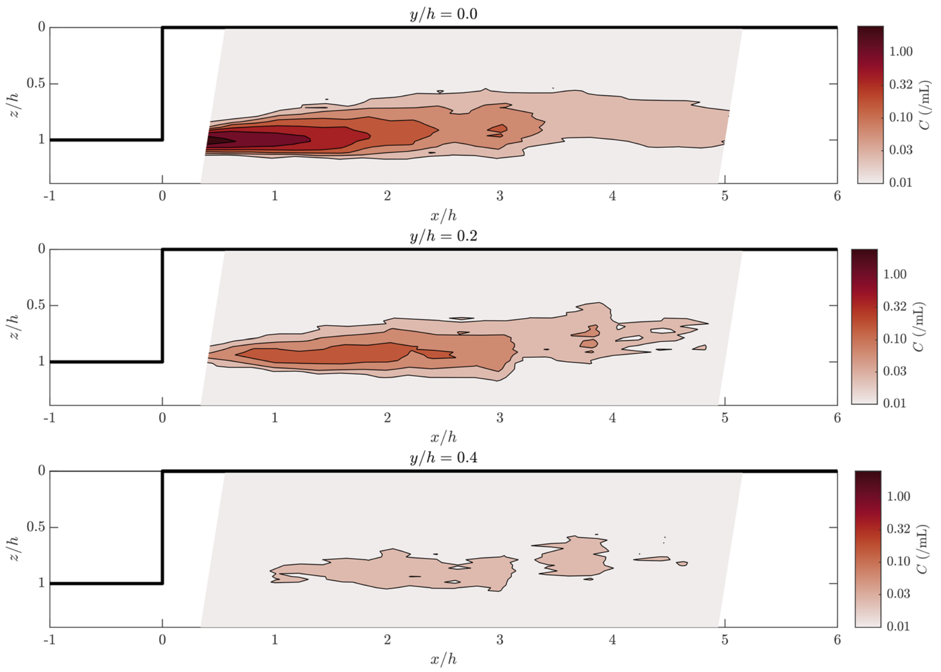

FIG. 18. Contour plots of bubble concentration in the wake of a BFS for three streamwise (x–z) planes at the spanwise locations $y = 0$, 2, and 4 h, obtained using the volumetric nuclei measurement technique based on Mie-scattering imaging. Contours indicate the region with highest concentration at the tunnel centerline just downstream of the step. The bubble concentration reduces with increase in spanwise and streamwise distance from the tunnel centerline and step, respectively. Note the logarithmic color bar and spacing between the contours.

consequent decrease in maximum concentration value in the $y = 0h$ plane. The maximum concentration value decreases about two orders of magnitude between the step and the most downstream measurement location.

The dispersion of the bubbly plume in spanwise directions is also evident in the contour plots of concentration distribution in the y–z planes. It can be seen that for the two most downstream planes ($x = 4$ and $5h$), the plume appears to contract; however, this is the result of very low bubble concentration in this region, which would require an impracticably large dataset to completely resolve.

VI. CAVITATION INCEPTION WITH MONODISPERSE SEEDING

Cavitation inception events were observed to occur in the cores of stretched quasi-streamwise vortices contained within the BFS shear layer. Injection of large nuclei resulted with an increase in the value of incipient cavitation number, $\sigma_i \approx 1.2$, in comparison with $\sigma_i \approx 0.65$ for the flow with the natural nuclei population. Inception at these higher σ values largely alleviated the issues related to secondary re-nucleation from the cavitation products and immediate formation of developed cavitation at σ_i for the flow with the natural nuclei population. Intermittency of inception enabled discrimination of individual events and assessment of the effect of σ and f_b on cavitation inception rate.

Dependence of the cavitation inception rate on σ for a constant nuclei injection rate, $f_b \approx 11$ kHz, is presented in Fig. 20 in a log–log plot. The results were obtained from the acoustic measurements acquired over a 60 s period at a sampling rate of 204.8 kHz. In addition to the hardware filtering, a 1–10 kHz bandpass filter was applied for processing of the acoustic data. A cavitation event was detected when acoustic pressure exceeds a threshold value set to 25 Pa. To ensure that

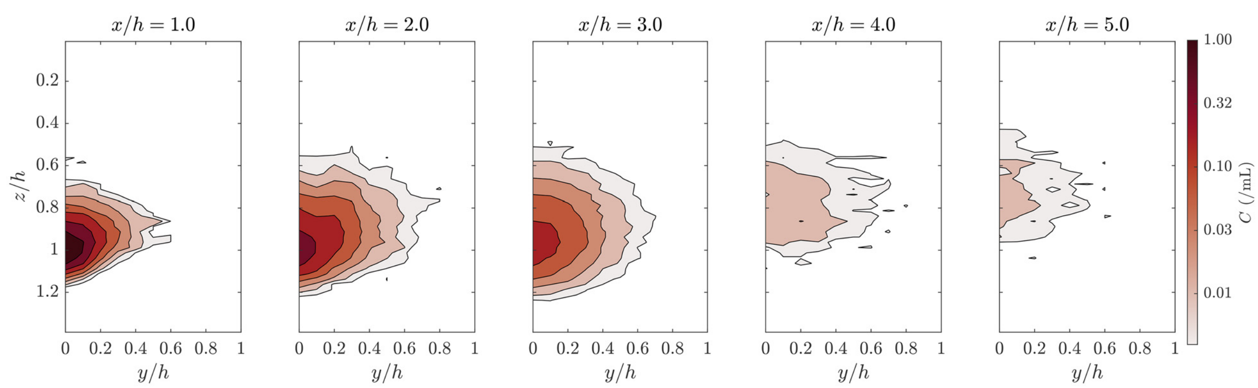

FIG. 19. Contour plots of bubble concentration in the wake of a BFS for five spanwise (y–z) planes at the streamwise locations $x = 1$, 2, 3, 4, and $5h$ downstream of the step, obtained using the volumetric nuclei measurement technique based on Mie-scattering imaging. Note the logarithmic color bar and spacing between the contours.

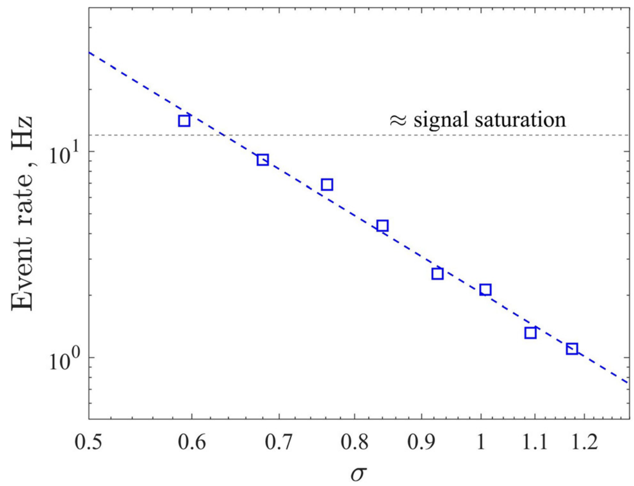

FIG. 20. Cavitation inception event rate as a function of cavitation number for a constant bubble injection rate ($f_b \approx 11$ kHz) presented in a log–log plot. Event rate increases following a power law with a decrease in σ as marked with a dashed line. The event rates are obtained from the acoustic measurements acquired over a time period of 60 s at a sampling rate of 204.8 kHz. The acoustic signal becomes saturated, i.e., individual events cannot be rigorously discerned, above the event rate of ≈12 Hz, as indicated with a dashed horizontal line in the plot.

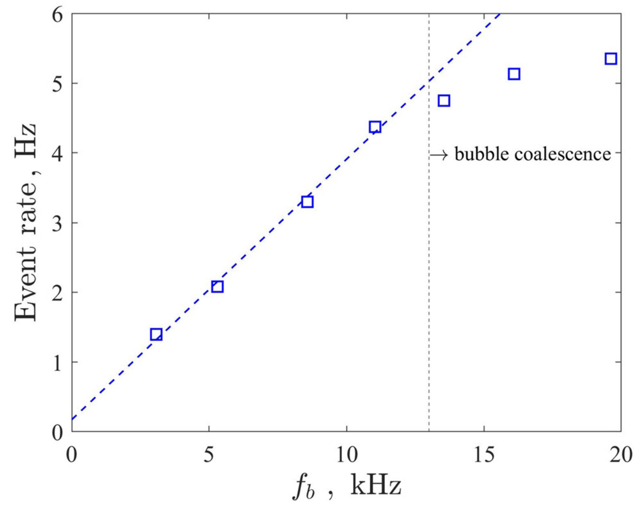

FIG. 21. Dependence of cavitation inception event rate on the bubble injection rate (f_b) for a constant cavitation number, $\sigma \approx 0.85$. Event rate increases linearly (represented with a dashed blue line) with an increase in f_b for $f_b \lesssim 13$ kHz. For the higher f_b values, the rate of increase reduces due to coalescence of large bubbles in the region just downstream of the injection port. The event rates are obtained from the acoustic measurements acquired over a time period of 60 s at a sampling rate of 204.8 kHz.

only individual events are captured, a minimum delay of 10 ms between the end of an event (acoustic pressure value decreasing below the threshold) and a start of a subsequent event was imposed.

Inception rate increases with a decrease in σ following a power law like behavior, as marked with a dashed blue line in Fig. 20. An event rate of ≈12 Hz is established as an upper limit for detection of individual events (dashed horizontal line), as for higher values, a time overlap between the individual events becomes more prominent. The measured event rate values of the order of 1 to 10 Hz, for the investigated σ range, demonstrate a low probability of a nuclei being captured in a vortex strong enough for activation to occur, with the probability being of the order of 0.01%–0.1%.

The gradual increase in the event rate with decreasing σ for the flow seeded with large monodisperse nuclei is in contrast with a step function at $\sigma \approx 0.65$ observed for the natural nuclei population, and is further evidence of the diminished influence of secondary re-nucleation on the cavitation inception in the seeded flow.

The influence of nucleation on cavitation inception was investigated by varying f_b for a constant σ. Cavitation event rate as a function of f_b is presented in Fig. 21 for $\sigma \approx 0.85$. Event rates are obtained from the acoustic measurements using the same processing as described above. A linear increase in the number of events is observed following an increase in the f_b up to $f_b \approx 13$ kHz. Above that value, the rate of increase reduces due to bubble coalescence in the region downstream of the injection port, as observed via shadowgraphy imaging.

The linear dependence of cavitation event rate on f_b indicates that at these higher σ values, the injected nuclei population is the only active population, and no natural nuclei are being activated. This is further evidenced with an observation that when the bubble injection is stopped, after a short period (order of a few seconds) required for depletion of the BFS re-circulation zone, cavitation completely disappears.

Scatterplots of the locations of incipient events in the x–z and x–y planes obtained from high-speed imaging are presented in Figs. 22 and 23, respectively, for $\sigma = 0.75$ and 1. These σ values were chosen to provide analysis for the conditions where only injected bubble population is active, i.e., there is no activation of the bubbles contained in the natural nuclei population. The scatterplots were populated using an algorithm based on examining the difference in the average pixel intensity of the consecutive frames from high-speed imaging from both cameras. If the difference between the pixel intensity of the two

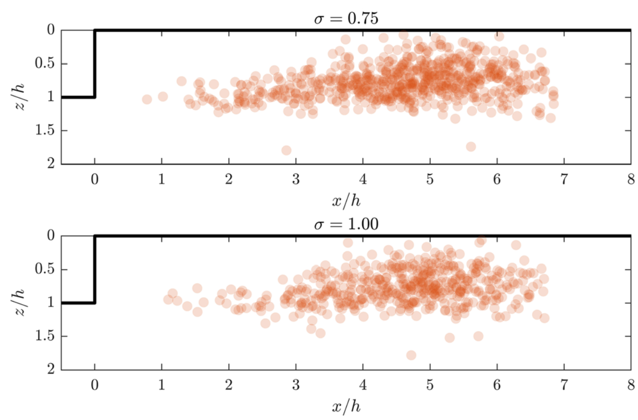

FIG. 22. Scatterplots of the locations of all inception events (along the y direction) captured in high-speed videos in x–z plane for $\sigma = 0.75$ and 1. Incipient events start to appear about h downstream of the step and have a peak in the density about 5h downstream of the step. Dispersion of the inception locations in $z-$ direction is related to the increase in the size of shear layer structures with increasing distance from the BFS. The BFS is represented with a thick black line in the upper left corner of the plots.

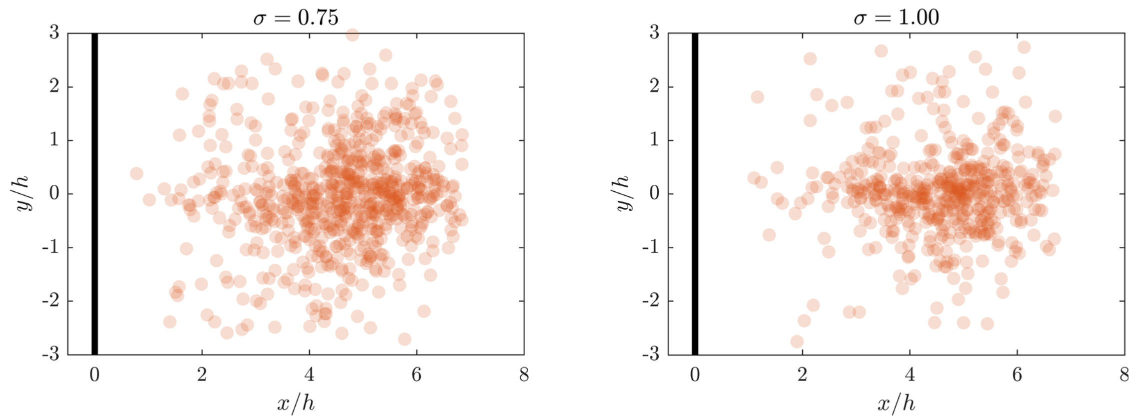

FIG. 23. Scatterplots of the locations of all inception events (along the z direction) captured in high-speed videos in x–y plane for $\sigma = 0.75$ and 1. High density of the events is evident within the dispersion boundaries of the plume of injected nuclei. However, a significant number of the events is recorded outside of the injected nuclei plume. The BFS is represented with a thick black line on the left side of the plots.

frames exceeded a threshold value, the location of the pixel with the highest intensity variation in the succeeding frame was recorded as the location of an incipient event. The threshold value was determined by examining the variation in the time series of pixel intensity of a high-speed video acquired for a non-cavitating condition ($\sigma = 4$). As cavities are represented with shadows, the threshold value was set 10-pixel intensity units lower than the minimum value recorded in the baseline time series. Overall, 681 and 492 events were detected in 61.7 and 100.3 s of the captured data, for $\sigma = 0.75$ and 1, respectively.

Distribution of the incipient events in x–z plane assumes the topology characteristic of the BFS shear layer, with a peak density in the region about $4 - 5h$ downstream of the step and $0.5 - 1h$ below the tunnel ceiling. Occasional outlying points at the vertical positions between $1.5h \leq z \leq 2$ were manually confirmed as cavitation events and are most likely attributable to the expulsion of vortical structures from the shear layer deeper into the freestream flow. The presented distributions are similar to those observed for the flow with a natural nuclei population as well as those reported by Agarwal *et al.* (2018).

Distribution of the incipient events in x–y plane has a region of maximum density coinciding with the boundaries of dispersion of the injected nuclei plume. However, a considerable number of events was detected outside of the plume region. This can be attributed to a gradual dispersion in the y direction of the injected bubbles and/or the bubbly products generated by cavitation that get captured within the step large re-circulation zone. While the MSI measurements indicate that bubbles remain within the plume, due to the timescales involved with the data acquisition, three dimensionality of the flow stemming from a step model with a moderate aspect ratio ($\approx$6) and large volume of re-circulation region, a very low concentration bubble population appears to disperse across the whole span of the step wake. While the bubble concentration outside of the plume is very low, it results with a notable number of cavitation events as the number of bubbles contained in this large volume is significant. The ratio of in and out of plume events appears to be consistent between the two σ values examined, suggesting that the phenomenon is not related to activation of the natural nuclei, i.e., no relative increase in the number of out of plume events was observed at the lower σ value. While the characterization of out of plume bubble population is within the capabilities of the MSI method used, due to extremely long time period required to acquire a statistically converged result, it was considered impracticable for this experimental campaign.

In order to reconcile the volumetrically continuous measurements of cavitation inception distribution and the discrete nuclei spatial distribution measurements, results have to be converted into mutually compatible discretized datasets. To do so, both datasets are discretized into cells $0.25h \times 0.25h \times 0.25h$ in x, y, and z directions. A sample dataset generated using this process is presented in Fig. 24. Mapping of spatial distribution of cavitation inception rate in the BFS shear layer for $\sigma = 0.75$ (a) and 1 (b) is shown discretized into 0.25 $\times\, 0.25h$ cells in x–z plane and for a $0.25h$ cell at the tunnel mid-span in y direction. A second order Savitzky–Golay digital filter is used to obtain a better estimate of the distribution from the sparse raw data. The discretized data shows a smooth distribution of cavitation events across the x–z center plane, with an approximately twofold increase in the number of events between the two σ values distributed uniformly across the cells. Additionally, the spatial distribution of the nuclei content discretized using the same grid is shown in the bottom of the image (c). A clear outline of the injected nuclei plume is observable in the discretized data.

From qualitative analysis, the spatial distribution of the incipient events in x–z plane for seeded flow presented in Figs. 22 and 24 is similar to the spatial distribution of cavitation activity for natural nuclei population shown in Fig. 7. This indicates that nucleation does not significantly affect the location of cavitation inception. Statistical comparison of the spatial distributions between the populations could not be determined due to the re-nucleation phenomenon described in Sec. IV.

Discretized cavitation inception data are presented in Fig. 25 as histograms of event rate spatial distribution in y direction for $\sigma = 0.75$ and 1. The histograms are presented for five spanwise planes located $x = 1$, 2, 3, 4, and $5h$ downstream of the step. Each $0.25h$ wide histogram box is obtained as the sum of all events in the vertical direction and $0.25h$ each side of the nominal x position of the plane. Additionally, the nuclei content distribution from the MSI measurements, averaged in the z direction, is shown for each plane. Note that the concentration axis of the MSI measurements has a logarithmic scale.

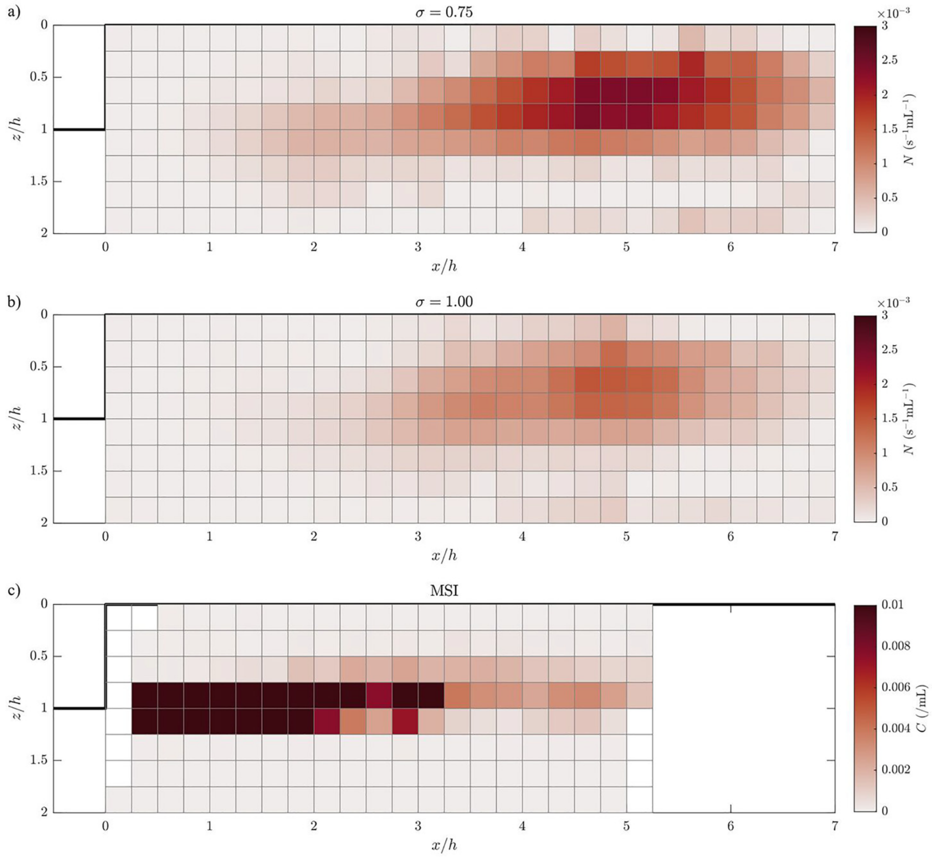

FIG. 24. Mapping of the spatial distribution of cavitation inception event rate in the BFS shear layer for $\sigma = 0.75$ (a) and 1 (b). The continuous volumetric data obtained using two high-speed cameras is discretized into cells $0.25 \times 0.25h$ in x–z plane and a $0.25h$ cell at tunnel mid-span in y direction. A second order Savitzky–Golay filter is used to smooth the raw data. Spatial distribution of the nuclei concentration discretized over the same grid is shown in the bottom of the figure (c). The BFS is represented with a thick black line in the upper left corner of the plots.

The histograms synthesize the observations from the scatterplots, showing the high density of the cavitation events within the plume boundaries and a considerable number of events outside of the plume. A twofold increase in the number of events between the two investigated σ values nominally uniformly distributed across the span can also be observed. While the maximum nuclei concentration reduces about two orders of magnitude between the most upstream and the most downstream plane, the number of cavitation events between these planes increases by approximately an order of magnitude, indicating a large increase in the cavitation susceptibility.

Discretized values of cavitation susceptibility can be calculated by dividing the discretized fields of cavitation inception event rates and nuclei concentrations. Sample mapping of the spatial distribution of cavitation susceptibility in the BFS shear layer in x–z plane for $\sigma = 0.75$ and 1 is presented in Figs. 26(a) and 26(b), respectively. Data are obtained by dividing the cavitation inception event rate with the nuclei concentration for each discretization point ($0.25 \times 0.25 \times 0.25h$ cell) and then averaging the value across the y direction. Averaging in the y direction may be performed as the flow is nominally two dimensional and, therefore, the ensemble average of the cavitation susceptibility (unsteady pressure field) should be representative of any plane across the span. To avoid division by zero for the cells where nuclei concentration is either zero or not measured, but inception events are observed, these are removed from the dataset.

Spatial distributions of cavitation susceptibility indicate a region of elevated susceptibility about $5h$ downstream of the step and $0.75h$ below the tunnel ceiling. Due to the limited field of view of current nuclei measurements system, the exact location of the peak in cavitation susceptibility as well as the decay of susceptibility downstream of the peak are not captured. The obtained distributions compare favorably with the mapping of cavitation susceptibility obtained experimentally by Agarwal *et al.* (2018) and numerically by Brandao and Mahesh (2022) for a step model one-tenth of the scale. From the high resolution time-resolved measurements of the pressure field in the BFS shear layer, Agarwal *et al.* (2020) relate the location of the peak in the cavitation susceptibility to the location of the peak in pressure fluctuations within the stretched QSVs.

Figure 26(c) represents the streamwise distribution of the averaged cavitation susceptibility summed in z direction for $\sigma = 0.75$ and 1. As expected, a decrease in σ results with an increase in the cavitation susceptibility across all the streamwise locations, while also extending the region susceptible to cavitation further upstream toward the step.

VII. CONCLUSIONS

Cavitation inception in a high Reynolds number shear layer formed in the wake of a backward-facing step was experimentally investigated in a water tunnel for two nuclei populations. Discrete

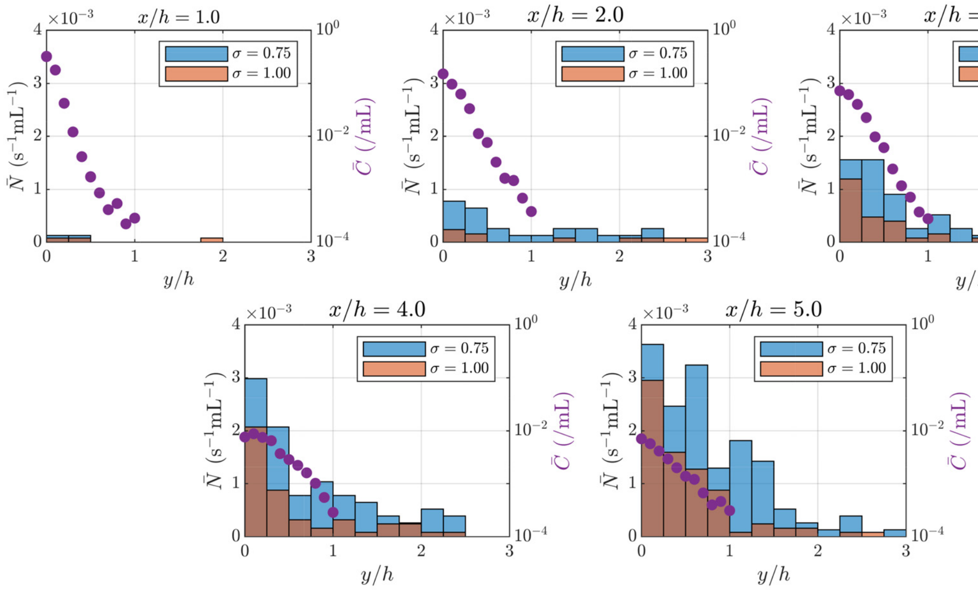

FIG. 25. Histograms of the cavitation inception event rate spatial distribution in y direction for $\sigma = 0.75$ and 1. Histograms are presented for y–z planes located at $x = 1$, 2, 3, 4, and 5h. Each value represents the sum of all events in the z direction and 0.25h each side of the nominal position of the plane in streamwise direction. Additionally, distribution of nuclei concentration from the MSI measurements (purple circles), averaged in z direction, is shown for each plane. Note the logarithmic scale of the concentration axis.

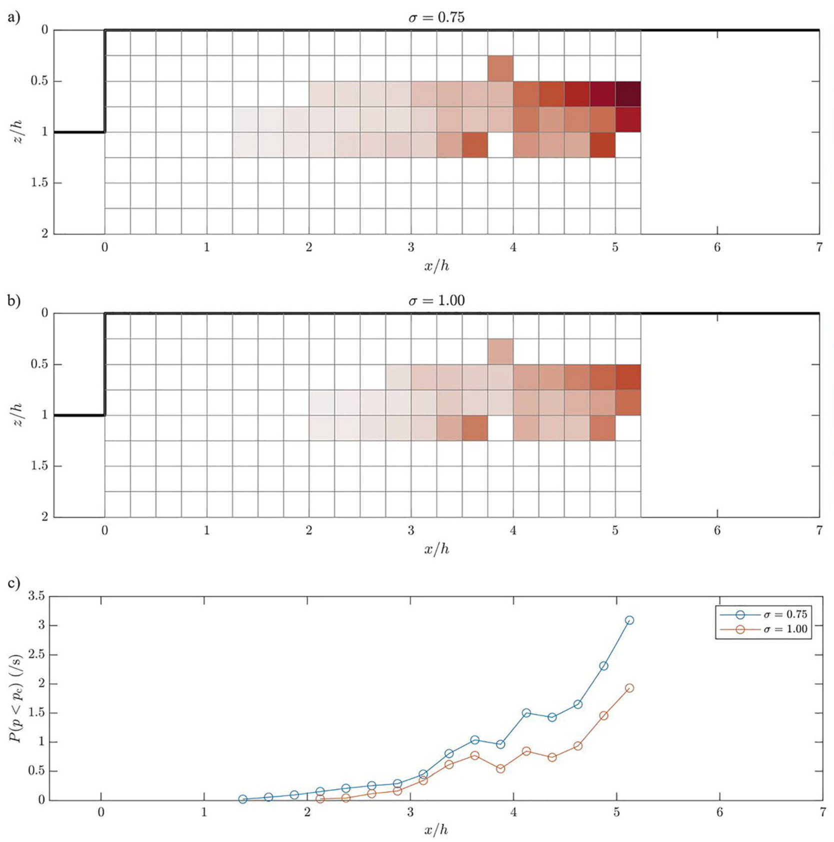

FIG. 26. Mapping of the spatial distribution of the cavitation susceptibility in the BFS shear layer in x–z plane for $\sigma = 0.75$ (a) and 1 (b). Cavitation susceptibility is obtained by dividing the cavitation inception event rate with the nuclei concentration for each discretization point ($0.25 \times 0.25 \times 0.25h$ cell) and then averaging the value across the tunnel span. The bottom plot (c) represents the x distribution of the sum of the averaged cavitation susceptibility in the z direction.

incipient cavities were observed in quasi-streamwise vortices in the shear layer, forming either spherical or stretched bubbly structures across a wide range of sizes.

For the natural nuclei population, it was observed that microbubbles generated during collapse and condensation of initial incipient events get captured within the step re-circulation zone, thus altering the local nuclei content. Generated microbubbles are often larger than those contained in natural nuclei population and act as preferential sites for re-nucleation, triggering a compounding effect and onset of developed cavitation. The effect of re-nucleation made statistical characterization of discrete incipient events impractical.

To alleviate the issues related to re-nucleation effects, targeted seeding of the flow with a population of large near monodisperse nuclei through a single point on a BFS model is utilized. Additionally, the spatial distribution of the nuclei was statistically characterized using a volumetric nuclei measurement technique based on MSI.

Seeding the flow with large nuclei largely addressed the issue of secondary re-nucleation of the BFS re-circulation zone by the products of the incipient cavitation events. However, detection of incipient events outside of the bubbly plume boundaries indicates that injected bubbles and/or cavitation products are still captured by the re-circulating flow and dispersed across the tunnel span. Three dimensionality of the flow stemming from a moderate step aspect ratio and the existence of a large re-circulation volume make the absolute control of the local nuclei content extremely challenging, and therefore, the use of a different model geometry would be beneficial. A geometry more suitable for nucleation experiment would need to be highly two dimensional without the tendency to capture and store nuclei in regions of re-circulating flow.

While some of the issues still remain unresolved, the obtained results show the inception to be a very rare event (only order of 0.01%–0.1% of nuclei becoming activated), depending on confluence of unlikely spatiotemporal probabilities—nuclei being captured by a vortex and the pressure in the vortex core being below the nuclei critical pressure.

The mapping of the spatial distribution of cavitation susceptibility, obtained by combining the cavitation inception and nuclei concentration maps, compares favorably with those reported for the same geometry in the literature. Therefore, current work provides a detailed dataset that is particularly valuable for the development of computational tools used for modeling of cavitation inception in nucleated flows.

ACKNOWLEDGMENTS

The authors wish to acknowledge the assistance of Mr. Robert Wrigley and Mr. Steven Kent in carrying out the experiments. The authors wish to acknowledge the support of the Australian Defence Science and Technology Group (contract number MyIP 8106) within the framework of the University of Tasmania collaborative work on Office of Naval Research 2017 U.S. Multidisciplinary University Research Initiative (MURI) entitled "Predicting turbulent multi-phase flows with high-fidelity: A physics-based approach" (program managers Dr. Ki-Han Kim and Dr. Yin Lu Young).

AUTHOR DECLARATIONS

Conflict of Interest

The authors have no conflicts to disclose.

Author Contributions

Elizabeth Samantha Clare Allan: Conceptualization (equal); Data curation (lead); Formal analysis (lead); Methodology (equal); Visualization (equal); Writing – original draft (lead); Writing – review & editing (lead). **Luka Barbaca:** Conceptualization (equal); Data curation (equal); Formal analysis (equal); Methodology (equal); Project administration (supporting); Supervision (equal); Visualization (supporting); Writing – original draft (equal); Writing – review & editing (equal). **James Venning:** Data curation (equal); Formal analysis (equal); Methodology (equal); Supervision (equal); Visualization (equal); Writing – original draft (supporting); Writing – review & editing (supporting). **Patrick Russell:** Data curation (supporting); Formal analysis (equal); Methodology (supporting); Visualization (equal); Writing – original draft (supporting); Writing – review & editing (supporting). **Bryce Pearce:** Conceptualization (equal); Data curation (equal); Formal analysis (equal); Funding acquisition (lead); Methodology (equal); Project administration (equal); Writing – original draft (equal); Writing – review & editing (equal). **Paul Brandner:** Conceptualization (lead); Data curation (equal); Formal analysis (equal); Funding acquisition (lead); Methodology (equal); Project administration (lead); Supervision (lead); Writing – original draft (equal); Writing – review & editing (equal).

DATA AVAILABILITY

The data that support the findings of this study are available within the article and its supplementary material.

REFERENCES

Agarwal, K., Ram, O., and Katz, J., "Cavitating structures at inception in turbulent shear flow," in Proceedings of the 10th International Symposium on Cavitation (CAV2018) (2018).

Agarwal, K., Ram, O., Wang, J., Lu, Y., and Katz, J., "Measuring the 3D pressure field and relating it to cavitation inception in a turbulent shear layer," in Proceedings of the 33rd Symposium on Naval Hydrodynamics (2020).

Agarwal, K., Ram, O., Wang, J., Lu, Y., and Katz, J., "Reconstructing velocity and pressure from noisy sparse particle tracks using constrained cost minimization," Exp. Fluids **62**, 75 (2021).

Arndt, R. E. A., "Cavitation in vortical flows," Annu. Rev. Fluid Mech. **34**, 143–175 (2002).

Barbaca, L., Paul, R. A., Brandner, P. A., and Pearce, B. W., "Microbubble production in a confined cavitating radial jet," in 11th International Symposium on Cavitation (2021).

Barbaca, L., Pearce, B. W., Ganesh, H., Ceccio, S. L., and Brandner, P. A., "On the unsteady behaviour of cavity flow over a two-dimensional wall-mounted fence," J. Fluid Mech. **874**, 483–525 (2019).

Belle, A., Brandner, P. A., Pearce, B. W., de Graaf, K. L., and Clarke, D. B., "Artificial thickening and thinning of cavitation tunnel boundary layers," Exp. Therm. Fluid Sci. **78**, 75–89 (2016).

Bernal, L. P. and Roshko, A., "Streamwise vortex structure in plane mixing layers," J. Fluid Mech. **170**, 499–525 (1986).

Brandao, F. L., Madabhushi, A., Bhatt, M., and Mahesh, K., "Large eddy simulation for the investigation of different regimes of cavitation," in Proceedings of the 33rd Symposium on Naval Hydrodynamics (2020).

Brandao, F. L. and Mahesh, K., "Large-eddy simulation of cavitation inception in a shear flow," Int. J. Multiphase Flow **146**, 103865 (2022).

Brandner, P., Lecoffre, Y., and Walker, G., "Development of an Australian national facility for cavitation research," in Sixth International Symposium on Cavitation-CAV 2006 (2006).

Brandner, P., Lecoffre, Y., and Walker, G., "Design considerations in the development of a modern cavitation tunnel," in *Proceedings of the 16th Australasian Fluid Mechanics Conference, 16AFMC* (University of Queensland, 2007), pp. 630–637.

Brandner, P. A., Venning, J. A., and Pearce, B. W., "Nucleation effects on cavitation about a sphere," J. Fluid Mech. **946**, A1 (2022).
Chang, N. A., Choi, J., Yakushiji, R., and Ceccio, S. L., "Cavitation inception during the interaction of a pair of counter-rotating vortices," Phys. Fluids **24**, 014107 (2012).
Doolan, C., Brandner, P., Butler, D., Pearce, B., Moreau, D., and Brooks, L., "Hydroacoustic characterization of the AMC cavitation tunnel," in Proceedings of Acoustic 2013 Victor Harbour, Australia (2013).
Franc, J. P. and Michel, J. M., *Fundamentals of Cavitation*, Fluid Mechanics and its Applications Vol. 76 (Kluwer Academic Publishers, Dordrecht, 2004).
Iyer, C. O. and Ceccio, S. L., "The influence of developed cavitation on the flow of a turbulent shear layer," Phys. Fluids **14**, 3414–3431 (2002).
Katz, J. and O'Hern, T. J., "Cavitation in large scale shear flows," J. Fluids Eng. **108**, 373–376 (1986).
Kermeen, R. W. and Parkin, B. R., "Incipient cavitation and wake flow behind sharp-edged disks," Hydrodynamics Lab Report No. 85-4 (California Institute of Technology, 1957).
Khoo, M. T., Venning, J. A., Pearce, B. W., and Brandner, P. A., "Statistical aspects of tip vortex cavitation inception and desinence in a nuclei deplete flow," Exp. Fluids **61**, 145 (2020a).
Khoo, M. T., Venning, J. A., Pearce, B. W., and Brandner, P. A., "Nucleation and cavitation number effects on tip vortex cavitation dynamics and noise," Exp. Fluids **62**, 216 (2021).
Khoo, M. T., Venning, J. A., Pearce, B. W., Takahashi, K., Mori, T., and Brandner, P. A., "Natural nuclei population dynamics in cavitation tunnels," Exp. Fluids **61**, 34 (2020b).
Lasheras, J. C., Cho, J. S., and Maxworthy, T., "On the origin and evolution of streamwise vortical structures in a plane, free shear layer," J. Fluid Mech. **172**, 231–258 (1986).
O'Hern, T. J., "An experimental investigation of turbulent shear flow cavitation," J. Fluid Mech. **215**, 365–391 (1990).
Russell, P. S., Barbaca, L., Venning, J. A., Pearce, B. W., and Brandner, P. A., "Measurement of nuclei seeding in hydrodynamic test facilities," Exp. Fluids **61**, 79 (2020a).
Russell, P. S., Barbaca, L., Venning, J. A., Pearce, B. W., and Brandner, P. A., "The influence of nucleation on cavitation inception in tip-leakage flows," in 34th Symposium on Naval Hydrodynamics (2022).
Russell, P. S., Venning, J. A., Brandner, P. A., Pearce, B. W., Giosio, D. R., and Ceccio, S. L., "Microbubble disperse flow about a lifting surface," in 32nd Symposium on Naval Hydrodynamics (2018).
Russell, P. S., Venning, J. A., Pearce, B. W., and Brandner, P. A., "Calibration of Mie scattering imaging for microbubble measurement in hydrodynamic test facilities," Exp. Fluids **61**, 93 (2020b).
Stramski, D., Boss, E., Bogucki, D., and Voss, K. J., "The role of seawater constituents in light backscattering in the ocean," Prog. Oceanogr. **61**, 27–56 (2004).
Temperley, H. N. V. and Chambers, L. G., "The behaviour of water under hydrostatic tension: I," Proc. Phys. Soc. **58**, 420–436 (1946).
Venning, J. A., Khoo, M. T., Pearce, B. W., and Brandner, P. A., "Background nuclei measurements and implications for cavitation inception in hydrodynamic test facilities," Exp. Fluids **59**, 71 (2018).
Venning, J. A., Pearce, B. W., and Brandner, P. A., "Nucleation effects on cloud cavitation about a hydrofoil," J. Fluid Mech. **947**, A1 (2022).
Zarruk, G. A., Henderson, A. D., de Graaf, K. L., Brandner, P. A., and Pearce, B. W., "Validation of a microbubble seeding generator for particle image velocimetry applications," in 19th Australasian Fluid Mechanics Conference (2014).